

# ENHANCED ABLATION BY FEMTOSECOND AND NANOSECOND LASER PULSES

by  
HALEY KERRIGAN  
B.A. Physics, Connecticut College, 2015  
B.A. Mathematics, Connecticut College, 2015

A thesis submitted in partial fulfillment of the requirements  
for the degree of Master of Science  
in the College of Optics and Photonics  
at the University of Central Florida  
Orlando, FL

Fall Term  
2017

Major Professor: Martin Richardson

© 2017 Haley Kerrigan

## ABSTRACT

Laser ablation of GaAs by a combination of femtosecond and nanosecond pulses is investigated as a means of enhancing material removal by a femtosecond pulse in the filamentation intensity regime. We demonstrate for the first time increased ablation of GaAs by ultrafast laser pulse plasmas augmented by nanosecond pulse radiation from a secondary laser. Material removal during laser ablation is a complex process that occurs via multiple mechanisms over several timescales. Due to different pulse durations, ablation by femtosecond and nanosecond pulses are dominated by different mechanisms. Ablation can be enhanced by optimally combining a femtosecond and nanosecond pulse in time. In this work, the craters generated by combinations of pulses are investigated for inter-pulse delays ranging from -50ns to +1 $\mu$ s, with the fs pulse preceding the ns pulse corresponding to a positive delay. The Ti:Sapph Multi-Terawatt Femtosecond Laser (MTFL) in the Laser Plasma Laboratory (LPL) provides 50fs pulses at 800nm with intensities of  $10^{14}$ W/cm<sup>2</sup> at the sample. An Nd:YAG laser (Quantel CFR200) provides 8ns pulses at 1064nm with intensities of  $10^9$ W/cm<sup>2</sup>. Crater profilometry with white-light interferometry and optical microscopy determine the structure and surface features of the craters and the volume of material removed. Ultrafast shadowgraphy of the ejected plasma provides insight to the dual-pulse ablation dynamics. Sedov-Taylor analysis of the generated shockwave reveals the energy coupled to the sample or preceding plasma. It was found that inter-pulse delays between +40 and +200ns yielded craters 2.5x greater in volume than that of the femtosecond pulse alone, with a maximum enhancement of 2.7x at +100ns. Shadowgraphy of -40 to +40ns delays revealed that enhancement occurs when the nanosecond pulse couples to plasma generated by the

fs pulse. This work provides a possible means of enhancing ablation by femtosecond filaments, which propagate long distances with clamped intensity, advancing long-range stand-off ablation.

## **ACKNOWLEDGMENTS**

I would like to thank my advisor, Dr. Martin Richardson, for the opportunity to conduct research at the College of Optics and Photonics as a member of the Laser Plasma Laboratory (LPL). His support and guidance have been critical to my success as student and researcher. His expertise in optics, lasers, and plasma physics were key to guiding me through planning and carrying out this project.

I would like to thank my committee members, Dr. Martin Richardson, Dr. Matthieu Baudelet, Dr. Bhimsen Shivamoggi, and honorary member Dr. Sherminéh Rostami-Fairchild, for their time and contributions.

I would also like to acknowledge Dr. Sherminéh Rostami-Fairchild, who provided ongoing support and advice during the planning, experiment, and writing components of this Master's Thesis. I am grateful for her leadership and experience in laser filamentation. Dr. Matthieu Baudelet also provided valuable guidance throughout this process.

I am very grateful for the support of my fellow members of LPL. The input and assistance of the Filamentation Team, particularly Danielle Reyes and Daniel Thul, helped me stay on track and solve problems throughout the experiment. I would also like to thank Dr. Cheonha Jeon, who made extra effort to make me comfortable in the lab and in LPL during my first year at UCF. This project would not have been possible without the efforts of the Laser Development Team, particularly Nathan Bodnar and Joshua Bradford, in designing and implementing MTFL.

I would like to thank Daniel Webber, who interned under me during the summer I conducted this experiment and was always ready to help even after long hours in the lab.

Finally, I want to thank my family for whole-heartedly supporting and encouraging me throughout the entirety of my education. My parents, John and Sue, have supported my education wherever it took me, taught me faith and the value of hard work, and always believed I was capable of accomplishing great things. My sisters, Katrina and Faith, constantly motivate me to be my best. I want to thank my best friend for his constant encouragement and standing by my side through many late nights and long hours. I am extremely grateful for all of the love and support I have received.

## TABLE OF CONTENTS

LIST OF FIGURES .....	ix
LIST OF TABLES .....	xi
LIST OF ABBREVIATIONS .....	xii
CHAPTER 1: INTRODUCTION .....	1
1.1 Motivation.....	1
1.2 Femtosecond Filamentation .....	4
1.2.1 Introduction.....	4
1.2.2 Physics of filamentation.....	5
1.2.2.1 Kerr self-focusing .....	5
1.2.2.2 Critical power and on-set of filamentation .....	6
1.2.2.3 Plasma generation and defocusing.....	7
1.2.3 Properties of filaments .....	9
1.2.3.1 Filament core .....	9
1.2.3.2 Energy reservoir.....	9
1.2.4 Ablation with filaments.....	10
CHAPTER 2: LASER ABLATION .....	13
2.1 Introduction.....	13
2.2 Laser Ablation Mechanisms .....	14
2.2.1 Nanosecond Ablation.....	14
2.2.2 Femtosecond Ablation .....	17
2.2.3 Double pulse ablation .....	19
2.2.3.1 Ns/ns ablation.....	19
2.2.3.2 Fs/fs ablation.....	20

2.2.3.3 Fs/ns ablation .....	20
CHAPTER 3: FACILITIES AND EXPERIMENTAL DETAILS .....	22
3.1 Lasers .....	22
3.1.1 Femtosecond laser source .....	22
3.1.2 Nanosecond laser source.....	23
3.2 Experimental set-up .....	24
3.3 Samples/Targets .....	24
3.4 Diagnostics.....	28
3.4.1 Laser Diagnostics.....	28
3.4.2 Sample Metrology.....	29
3.4.3 Shadowgraphy.....	29
CHAPTER 4: ABLATION WITH FS-NS DUAL PULSES .....	31
4.1 Experimental Results .....	31
4.1.1 Sample Metrology.....	31
4.1.1.1 Zygo results.....	32
4.1.1.2 Optical microscopy .....	37
4.1.2 Shadowgraphy.....	42
4.2 Discussion of ablation enhancement mechanisms.....	47
CHAPTER 5: CONCLUSION .....	51
REFERENCES .....	52



## LIST OF FIGURES

Figure 1. Illustration of processes involved in laser filamentation. ....	5
Figure 2. Colorized CCD image of a femtosecond filament (a) and a corresponding intensity line out (b) highlighting the filament core (yellow) and surrounding energy reservoir (red).....	9
Figure 3. Focusing regimes investigated by Valenzuela et al [3]. ....	11
Figure 4. Comparison of the intensity profile of a filament (top) and a single-shot ablation crater in GaAs (bottom) [29].....	12
Figure 5. Overview of the processes and timescales involved in ablation by a (a) nanosecond and (b) femtosecond pulse. ....	14
Figure 6. Cartoon illustrating some of the processes involved in (a) nanosecond and (b) femtosecond laser ablation.....	17
Figure 7. Simplified schematic of MTFL. ....	23
Figure 8. Schematic of experimental set-up. ....	24
Figure 9. Oscilloscope traces of fs-ns dual pulses. ....	25
Figure 10. Beam profiles of the fs (a) and ns (c) beams at focus and lineouts showing their respective normalized intensity profiles (b and d). ....	26
Figure 11. Simplified illustration of shadowgraphic imaging. ....	30
Figure 12. Schematic of the shadowgraphy technique with the pump-probe setup. ....	30
Figure 13. Volume of the ablation crater as function of inter-pulse delay (black squares). The red and blue dotted lines represent the volumes removed by a single fs pulse and single ns pulse (not a function of delay). The pink dotted line is the calculated sum the single fs and single ns volumes. The data is shown on a zoomed in (a) and a zoomed out (b) timescale. ....	33
Figure 14. Sample crater profiles showing size and depth for different inter-pulse delays. The delay in ns is given in bold above the profile. The profiles in the black box (top-left) are from a single fs and single ns pulse.....	34
Figure 15. Lineouts across the craters generated by a single fs (a) and single ns (b) pulse. The pictures on the right indicate where the lineouts were taken. ....	35
Figure 16. Lineouts across crater profiles for inter-pulse delays of -40ns (a), -10ns(b), 0ns (c), 10ns(d), 40ns(e), 80ns(f), 100ns(g), 150ns(h). ....	37

Figure 17. Optical microscope images of craters generated by single fs (a) and single ns (b) pulses. The images on the far left and far right are zoomed in to show details. ....	38
Figure 18. Optical microscope images of craters generated by different inter-pulse delays (a-f). The images on the far left and far right are zoomed in to show detail. The text on the far right indicates the inter-pulse delay.....	41
Figure 19. Diagram showing the regions of the expanding plasma and shockwave. ....	42
Figure 20. Select shadowgraph images of the expanding shockwave and plasma for single fs (a) and single ns (b) pulses. ....	43
Figure 21. Longitudinal shockwave radius as a function of time for single fs (blue) and single ns (red) pulses with fits of the Sedov-Taylor equation (blue and red dashed lines.) The image illustrates the measured radius of the shockwave. ....	44
Figure 22. Select shadowgraph images showing the expansion of the shockwave and plasma for inter-pulse delays between -40 and +40ns (a-g, see text on far right). The timing of the probe (relative to the fs pulse) is given below each image. ....	46
Figure 23. Longitudinal shockwave radius as a function of time for the ns pulse at +40ns inter-pulse delay (green) compared to the single ns pulse (red) with fits of the Sedov-Taylor equation (green and red dashed lines). The image illustrates the measured radius of the shockwave for the delayed ns pulse .....	47

## **LIST OF TABLES**

Table 1. Optical and thermal properties of GaAs at room temperature. ....	28
---	----

## LIST OF ABBREVIATIONS

AOM	Acousto-optic modulator
AOPDF	Acousto-optic programmable dispersive filter
Barium borate	BBO
CCD	Charge coupled device
CPA	Chirped pulse amplification
CW	Continuous wave
DDG	Digital delay generator
Fs	Femtosecond
IBA	Inverse Bremsstrahlung absorption
LIBS	Laser induced breakdown spectroscopy
LPL	Laser Plasma Laboratory
MPI	Multi-photon ionization
MTFL	Multi-Terawatt Femtosecond Laser
Ns	Nanosecond
NA	Numerical aperture
PI	Photo-ionization
Ps	Picosecond

# CHAPTER 1: INTRODUCTION

## 1.1 Motivation

The laser has become a critical tool in science, industry, and defense since its invention. The spatial coherence, temporal confinement, and tunable monochromaticity of laser light make it ideal for materials processing. At low fluences, lasers can be used for heat treatment of surfaces. At high fluences, if the intensity exceeds the ablation threshold, material is removed. Some applications of laser ablation include drilling for industrial purposes, surgical cutting and thermotherapy treatment in medicine, laser induced breakdown spectroscopy (LIBS) for chemical and elemental analysis, cleaning delicate pieces of art, and space debris removal [1, 2, 3, 4, 5]. Ablation from a distance could greatly expand the applications of laser ablation and provide more flexibility within its current applications. Advances in laser technology yielding higher powers and shorter pulses make it possible to propagate intensities above the ablation threshold of most materials to great distances through femtosecond (fs) filamentation. There are still challenges, however, in removing significant amounts of material with filaments. Many fields would benefit from improved ablation efficiency of pulses in the filamentation intensity regime.

Femtosecond filamentation occurs when an fs pulse propagating in a non-linear medium, such as air, has sufficient peak power to self-focus and generate a weak plasma that in turn defocuses the beam. The balance of self-focusing and plasma defocusing generates a robust pulse that can propagate long distances with a clamped intensity several orders of magnitude above the ablation threshold of most materials at  $\sim 10^{14} \text{W/cm}^2$  throughout propagation [6]. Filamentation has been observed at distances over 1km during long-range propagation of high-intensity pulses [7]. Ablation with fs filaments offers several advantages and disadvantages over conventional

ablation techniques. Typical ablation techniques involve tightly focusing a beam to a small spot on the sample to achieve high intensities. The required high numerical aperture (NA) to achieve such intensities limits stand-off capabilities. The unique properties of filaments have been shown to yield consistent ablation rates at long distances [8, 9]. The ablation rate, however, is greater for focused beams that can achieve higher intensities through tight focusing and smaller spot sizes. Additionally, the clamping of intensity means the ablation rate of a single filament cannot be altered by changing the laser energy [10]. Advancing stand-off ablation thus relies on enhancing the rate of ablation of pulses in the filamentation intensity regime.

A way of improving the efficiency of laser ablation is by using a double pulse configuration. These configurations involve either splitting the pulse from one laser into two pulses with a controlled delay or using the outputs from two different lasers. In both cases, the ablated volume is larger for two pulses compared to a single pulse with equivalent energy. The reasons for improved ablation rate are complex but are thought to result from better energy coupling to the sample inducing more ablation and/or better removal of debris that was ablated but would otherwise be redeposited inside the ablation crater. Laser ablation involves a combination of optical, thermal, and mechanical processes that depend strongly on the pulse duration, laser energy, propagation medium, and target material. Material ablation in the regime of two pulses is naturally more complicated making optimization complex. The mechanisms for enhanced material removal in a double pulse configuration depends strongly on the spatial and temporal configuration of the double pulse.

Dual-pulse ablation with fs and nanosecond (ns) pulses has the potential for high ablation rates. This configuration has primarily been investigated for improving the atomic line signal in LIBS experiments. In some experiments, following an fs pulse with an ns pulse enhanced the

amount of ablated material, which contributed to a better signal [11, 12]. In these experiments, however, the inter-pulse delay typically ranges from one to hundreds of microseconds, where the principle contribution of the second pulse is increasing the number of excited ions already liberated from the surface to increase the atomic line signal. To maximize ablation, on the other hand, the second pulse should come sooner to utilize the residual thermal and plasma dynamics from the fs pulse. Many of the processes involved in material removal occur nanoseconds after the pulse interacts with the sample (see Ch. 2). In this regime, more energy from the second pulse can go directly into removing material.

The focus of this work is an fs-ns dual-pulse configuration temporally designed to improve the overall ablation of an fs pulse in the filamentation intensity regime. The inter-pulse delay is optimized for maximum material removal in a single shot. This work aims to answer the following questions:

1. How do femtosecond filaments interact with materials?
2. Can the laser ablation rate be improved with an auxiliary nanosecond pulse?
3. Can the timing of the pulses be optimized for maximum material removal?
4. What are the physical mechanisms leading to improved ablation?

This document is organized to provide the reader with a general understanding of fs laser pulse phenomena and laser ablation by fs and ns pulses so the above questions can be answered. The following section will describe the physics and properties of femtosecond filamentation. Chapter 2 will provide an introduction to laser ablation with emphasis on the physics of fs and by ns laser ablation and double pulse ablation. This will provide the background for the experiment, which is described in Chapter 3. The results and discussion are included in Chapter 4. Finally, in

Chapter 5 the results are summarized with an emphasis on potential applications and suggestions for further investigations.

## **1.2 Femtosecond Filamentation**

### **1.2.1 Introduction**

Filamentation has attracted much attention due to its widespread applications including remote sensing, communication, and weather control. The filament's distinctive properties, such as its unique intensity profile and ability to propagate long distances with a clamped intensity, make it attractive for many stand-off applications. Filamentation occurs when the peak power of a laser pulse exceeds the critical threshold value for a Kerr medium (10 GW in air at 800nm and 100fs pulse duration) [13]. At these power levels, the optical non-linearity of the medium causes the refractive index to increase on axis as a result of the optical Kerr effect. Self-focusing of the beam ensues and the resulting high on-axis intensity generates a plasma via multi-photon ionization that in turn lowers the local refractive index and defocuses the beam. This dynamic balance between Kerr self-focusing and plasma defocusing clamps the intensity of the beam at  $\sim 10^{14} \text{W/cm}^2$ , allowing the propagation of high intensities distances much greater than the Rayleigh range [6]. This focusing-defocusing cycle generates an intense filamentary plasma core



surrounded by a low intensity peripheral field or energy reservoir [14]. The following sections further describe the physical mechanisms of femtosecond filamentation.

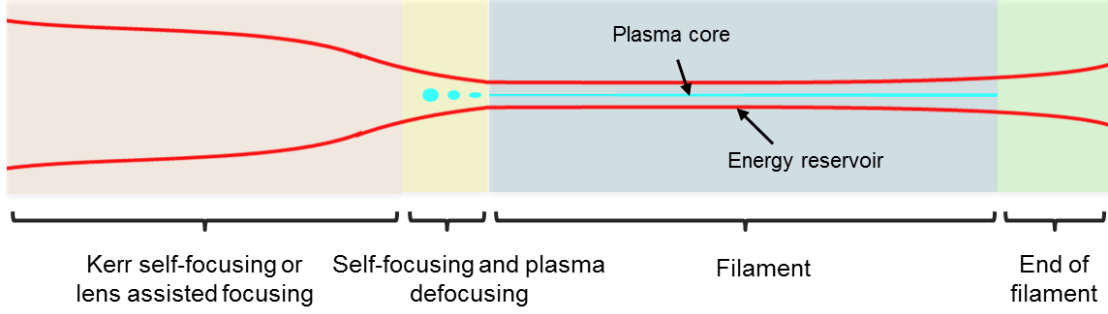


Figure 1. Illustration of processes involved in laser filamentation.

## 1.2.2 Physics of Filamentation

### 1.2.2.1 Kerr self-focusing

The change in refractive index induced by a laser beam propagating in a nonlinear medium is given by [6, 15]:

$$n(r, t) = n_0 + n_2 I(r, t) \quad (1.1)$$

where  $n_0$  is the linear refractive index of the medium,  $n_2$  is the second-order nonlinear refractive index, and  $I(r, t)$  is the radial and temporal intensity distribution of the beam. The nonlinear index is determined by third order susceptibility  $\chi^{(3)}$  of the propagation medium, the permittivity of free space  $\epsilon_0$ , the speed of light in a vacuum  $c$ , and  $n_0$  through [6, 16]:

$$n_2 = \frac{3\chi^{(3)}}{4\epsilon_0 c n_0^2}. \quad (1.2)$$

Air has a nonlinear index of  $3 \times 10^{-19} \text{cm}^2/\text{W}$  [17]. As evident from Equation 1.1, a beam with high optical intensity will significantly change the refractive index of a nonlinear medium. For Gaussian beams, the center of the beam with higher intensity experiences a greater change in refractive index than the edge, which has lower intensity. This radial distribution of refractive index acts like a positive lens, leading to Kerr self-focusing. When the beam has enough power to overcome diffraction, the pulse collapses into a filament.

#### *1.2.2.2 Critical power and on-set of filamentation*

With  $n_2$  being much smaller than  $n_0$ , significant intensities are required to induce a large enough change in refractive index for Kerr self-focusing. Furthermore, even greater intensity is required to overcome diffraction such that Kerr self-focusing and plasma defocusing are balanced, leading to the collapse of the pulse. The critical power is the threshold power required to induce the balance Kerr-self focusing and diffraction leading to collapse of the pulse. The critical power  $P_{cr}$  depends on the central wavelength  $\lambda_0$ , linear and nonlinear refractive indices, and a constant  $\alpha$  determined by the pulse's spatial profile. It is given by [6, 18]:

$$P_{cr} = \frac{\alpha \lambda_0^2}{4\pi n_0 n_2}. \quad (1.3)$$

For a CW Gaussian beam with a central wavelength of 800nm, the critical power air is 3.2 GW in air [6]. The location of the point of collapse can be estimated by the Marburger equation [18]:

$$z_c = \frac{0.184w_0^2k_0}{\sqrt{\left(\left(\frac{P}{P_{cr}}\right)^{\frac{1}{2}} - 0.853\right)^2 - 0.0219}} \quad (1.4)$$

where  $P_{cr}$  is the critical power,  $P$  is the input power,  $k_0$  is the wavenumber, and  $w_0$  is the Gaussian beam waist. While Equation 1.4 describes a CW beam, it is useful for approximating the point of collapse for pulsed sources [19]. While filamenting beams will collapse without any focusing optics, a focusing lens can induce collapse sooner. The onset of focus assisted collapse  $z_f$  with a lens of focal length  $f$  is given by [6]:

$$\frac{1}{z_f} = \frac{1}{f} + \frac{1}{z_c}. \quad (1.5)$$

It should be noted that if collapse is assisted by focusing with an NA high enough such that geometric focusing dominates over nonlinear focusing, the resulting plasma will be short, unstable, and dominated by linear processes and thus should not be considered a filament [20]. The minimum assisting focal length to be in the nonlinear focusing regime depends on the nonlinear medium, pulse duration, and pulse energy that determine the relative strengths of the geometric focusing, Kerr self-focusing, and plasma defocusing. For a single fs filament at 800nm in air, the transition to nonlinear focusing typically occurs around 0.003-0.005 NA.

### 1.2.2.3 Plasma generation and defocusing

A laser pulse with sufficient intensity will ionize air molecules generating a plasma. For a pulse at 800nm in air with intensity greater than the ionization threshold of  $\sim 10^{13} \text{W/cm}^2$ , plasma

generation occurs via multi-photon ionization (MPI) and tunneling ionization. In MPI, molecules with ionization potentials greater than the energy of a single photon become ionized by absorbing multiple photons. The primary constituents of air,  $O_2$  and  $N_2$ , have ionization potentials of 12eV and 15.6eV, respectively. Ionization of oxygen thus occurs first by absorbing 8 photons at 800nm. For self-focusing lasers that produce high on-axis intensity, tunneling ionization occurs from perturbations of the potential of the molecule by the strong incident electric field. For fs pulses, the plasma can be assumed to have an equal number of electrons and ions and the change in refractive index  $n_p$  from the plasma can be described by the Drude model [21]:

$$n_p = -\frac{\rho(r, t)}{2\rho_c}, \quad (1.6)$$

where  $\rho$  is the density of free electrons with respect to radial position and time and  $\rho_c$  is the critical plasma density. The critical plasma density,  $\sim 1.7 \times 10^{21} \text{cm}^{-3}$  for an 800nm pulse in air, is the density at which the plasma becomes opaque to incident light [6]. It is given by:

$$\rho_c = -\frac{\epsilon_0 m_0 \omega_0^2}{e^2}, \quad (1.7)$$

where  $e$  and  $m_0$  are the electron charge and mass,  $\epsilon_0$  is the permittivity in a vacuum, and  $\omega_0$  is the laser frequency. The negative change in refractive index given by Equation 1.6 creates an index gradient that acts like a negative lens and defocuses the beam. With sufficient power, the diverging beam will refocus via Kerr self-focusing and continue to experience plasma defocusing and self-focusing until a stable filament is formed with a clamped intensity at  $\sim 10^{14} \text{W/cm}^2$  [6]. The

filament ends when there is not enough power to overcome plasma defocusing. The main loss of power is due to MPI [6].

### 1.2.3 Properties of Filaments

#### 1.2.3.1 Filament core

When a pulse collapses to a filament it takes on a Townesian intensity profile consisting of a high intensity core surrounded by a lower intensity energy reservoir. The high intensity core generates a plasma channel that is 100-200 $\mu\text{m}$  (FWHM) in diameter and lasts the duration of the filament. Figure 2 shows an intensity profile taken with a CCD and a corresponding intensity lineout showing the Townesian profile. The high intensity center and low intensity outer lobes make up the core and energy reservoir.

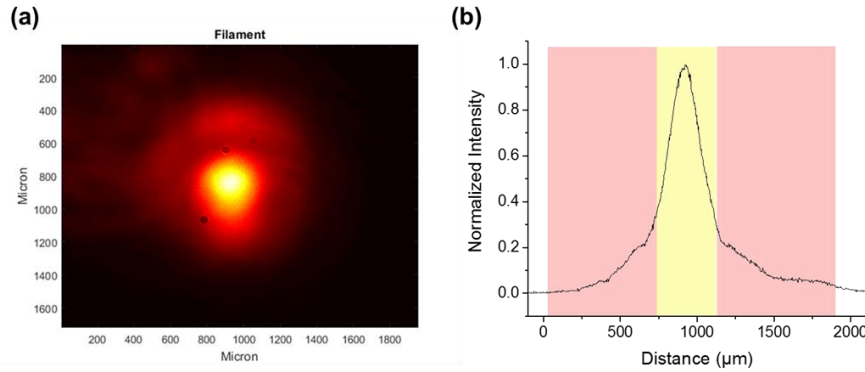


Figure 2. Colorized CCD image of a femtosecond filament (a) and a corresponding intensity line out (b) highlighting the filament core (yellow) and surrounding energy reservoir (red).

#### 1.2.3.2 Energy reservoir

The energy reservoir is known to play a crucial role in the formation and propagation of laser filaments, estimated to contain 50-90% of the total energy [22, 23, 24, 25]. Appearing as a

diffused halo of illumination, the reservoir is 5-10 times larger in size than the 100-200 $\mu$ m filament core [22, 25]. Experiments have demonstrated that because of this peripheral field, filaments are able to survive interaction with water droplets and other obstacles [26, 25, 27]. Additionally, self-healing properties attributed to the energy reservoir allow filaments to recover and improve symmetry after collisions [28]. While the intensity is low compared to the core, the energy reservoir is critical to the robustness of the filament.

#### 1.2.4 Ablation with Filaments

The properties of filaments have several effects on the material removal during laser ablation. These effects become apparent when comparing the ablation craters of a self-focused filament, focus assisted filament, and focused fs laser as described by Weidman and also Valenzuela *et al* [8, 9]. These regimes are illustrated in Figure 3. The investigation revealed the self-focused filament was the least efficient at removing material, while the focused beam (non-filament) was the most efficient [8]. The discrepancy is a result of intensity clamping during filamentation, meaning the tightly focused beam had a higher intensity at the sample. Intensity clamping, on the other hand, produces consistent ablation rates at long distances as fluctuations in energy are self-corrected during filament propagation [29].

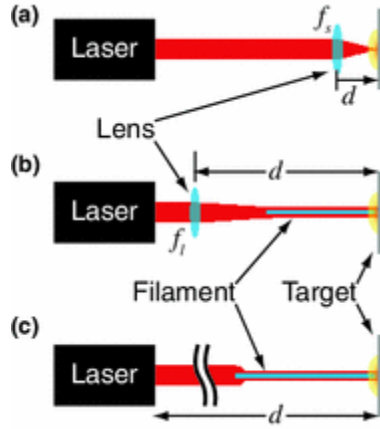


Figure 3. Focusing regimes investigated by Valenzuela *et al* [3].

Because of intensity clamping and the structure of the filament, increasing the energy does not increase the ablation rate. Xu *et al* showed that increasing the power of the laser did not increase the ablation rate of a metallic sample [10]. For 50fs pulses at 800nm, the number of shots required to penetrate aluminum foil did not change when the energy was increased from 360 to 800 $\mu$ J. They determined the 360 $\mu$ J cut-off energy corresponded to a peak power equal to the critical power for self-focusing with their conditions. This effect is supported by the work of Weidman who compared the structure of the crater with the intensity profile of the filament (Figure 4) [29]. This analysis revealed that the intensity of the energy reservoir was below the ablation threshold of the material and thus did not significantly affect the ablation crater. Another means of improving the ablation rate by a single filament is needed.

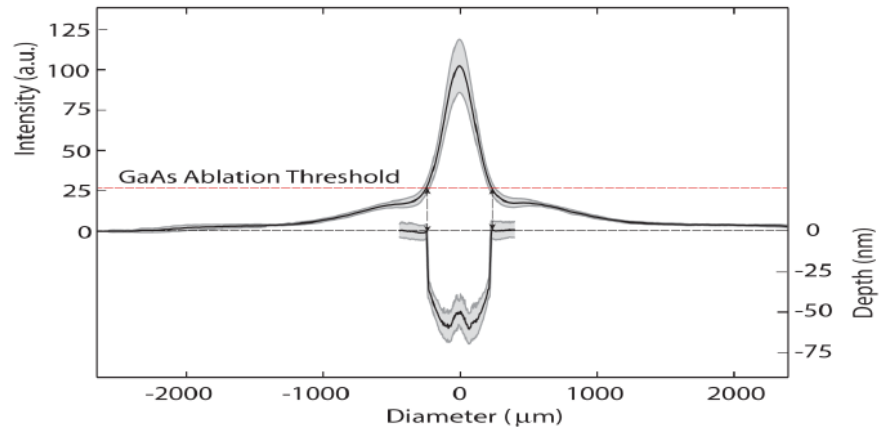


Figure 4. Comparison of the intensity profile of a filament (top) and a single-shot ablation crater in GaAs (bottom) [29].



## CHAPTER 2: LASER ABLATION

### 2.1 Introduction

Advances in ultrashort laser technology have made laser ablation important to many industrial and scientific applications. Lasers offer many advantages over traditional tools and techniques including speed, precision, tunability, and stand-off operation. The advantages and versatility of lasers makes laser ablation useful for a wide variety of fields and applications. Controlling properties of the incident light such as wavelength, energy, and pulse duration can yield a variety of outcomes that are ideal for different applications.

Ablation occurs when a material absorbs enough energy to be melted or vaporized. Material is removed when sufficient laser energy is coupled to the surface. The process of material removal can involve a combination of processes depending on the pulse duration, fluence, and wavelength of incident light and the optical, electrical, and thermal properties of the material. The dominant mechanisms determine the nature of the removed material, which can include atoms, ions, molecules, nanoparticles, clusters, and droplets. The forms of ablated material, in turn, determine the amount of material removed [30]. The removal of material can occur over different timescales. While photon-electron interactions occur nearly instantaneously with the pulse, several ionization, thermal, and mechanical processes leading to ablation can occur over longer timescales. Ablation by fs and ns pulses thus involve different mechanisms and are described in separate sections. Figure 5 compares the dominant processes and the timescales over which they occur. In high repetition rate or double pulse experiments, understanding these processes and timescales is critical to maximizing the amount of ablated material.

## 2.2 Laser Ablation Mechanisms

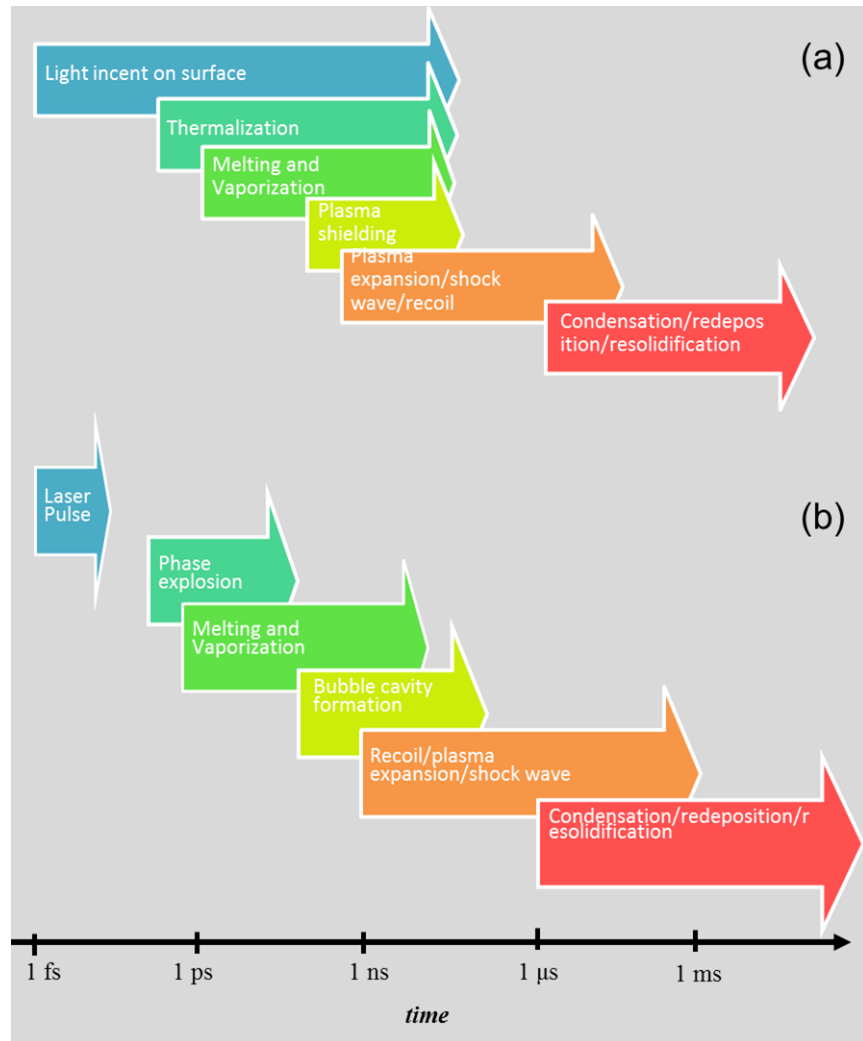


Figure 5. Overview of the processes and timescales involved in ablation by (a) nanosecond and (b) femtosecond pulse.

### 2.2.1 Nanosecond Ablation

For ns pulses, thermal vaporization is the dominant ablation process for irradiances on the order of or less than  $10^8 \text{ W/cm}^2$ . Thermalization of the electrons excited by the incident light occurs by electron-electron collisions on timescales of  $\sim 1 \text{ ps}$ , followed by energy transfer to the lattice via

phonon-electron relaxation over tens to hundreds of ps [31]. Because the pulse duration is much longer than the electron cooling time which is on the order of ps, the electrons and the lattice are considered to be in thermal equilibrium ( $T_e=T_l=T$ ) [32, 33]. A transition from solid to liquid to vapor leads to thermal vaporization over timescales of hundreds of ps to ns. The temperature distributions induced by the absorption of laser radiation by a material depend on the optical absorption within the irradiated zone, transport of heat out of this zone, and transformation enthalpies for phase changes and chemical reactions. This distribution is described by the heat equation. The heat equation in its general form is given by [30, 32, 33]:

$$q(T)c_p(T)\frac{\partial T(\mathbf{x},t)}{\partial t} - \nabla[k(T)\nabla T(\mathbf{x},t)] + q(T)c_p(T)\mathbf{v}_s\nabla T(\mathbf{x},t) = Q(\mathbf{x},t) \quad (2.1)$$

where  $q$  is the mass density,  $c_p$  is the specific heat,  $k$  is the thermal conductivity,  $\mathbf{v}_s$  is the substrate velocity relative to the heat source, and  $Q$  is the heat source in  $\text{W}/\text{cm}^3$ . Assuming all the light absorbed by the substrate is transformed into heat,  $Q$  can be written in terms of the time averaged Poynting vector (i.e. power flow of the light). The Lambert-Beer law tells the absorbed energy per second per volume as a function of intensity and absorption coefficient  $\alpha$  [30, 33]:

$$Q(x,t) = -\frac{dI(x,t)}{dx} = \alpha I(t) \exp(-\alpha x). \quad (2.2)$$

Additional energy may be required for phase changes or chemical reactions and can also be included in  $Q$  if necessary. Assuming  $q$ ,  $c_p$ ,  $k$  are linear with  $T$ , the substrate is stationary, and ignoring lateral heat expansion, the temperature in the sample is described by the 1-D heat equation [30]:

$$\frac{\partial T(x, t)}{\partial t} = \frac{\partial}{\partial x} \left[ \left( \frac{k}{qc_p} \right) \frac{\partial T(x, t)}{\partial x} \right] + \frac{\alpha}{qc_p} I(t) \exp(-\alpha x). \quad (2.3)$$

Equation 3.3 is a good approximation as long as the beam diameter is much greater than the penetration depth. The thermal processes in ns ablation result in a heat affected zone (HAZ) surrounding the crater [30].

Thermal vaporization can result in a high temperature plasma that exerts a recoil pressure on the surface of sample to conserve momentum during evaporation [30]. In focused ns ablation, the recoil pressure expels molten material out of region of interaction. This process of liquid phase expulsion removes increasing amounts of material with increasing laser intensity due to higher recoil pressures from increased vaporization. This process leaves raised edges surrounding the crater. The cooling and freezing of stress waves in the molten material can also produce raised features [34].

The material ejected during ns ablation can travel at supersonic velocity generating shockwaves that (i) expand into the ambient medium and (ii) secondly into the solid material. Shockwaves are produced when the region of air in front of the ejected material becomes compressed and heated. The high pressure generates a shockwave that expands outward away from the sample. Concurrently, the heat wave in the ablation zone exerting high pressures on the cold material sends a shockwave into the sample that can remove more material [30, 35].

Nanosecond ablation can be inefficient if a large portion of the pulse energy is not absorbed by the sample due to plasma shielding. While the energy coupled to plasma still aids in the evaporation process, the amount of material removed is much smaller compared to the initial part of the interaction. The light is mainly absorbed by the plasma through free electron-ion interactions

via inverse Bremsstrahlung absorption (IBA) [36, 37]. After sufficient absorption by IBA as well as single and multi-photon ionization, avalanche ionization can occur leading to optical breakdown of the plasma. Optical breakdown occurs when the plasma is sufficiently ionized such that it prevents laser light from reaching the sample. As the plasma expands and cools, condensation leads to the formation of particles and droplets that are deposited in and around the crater.

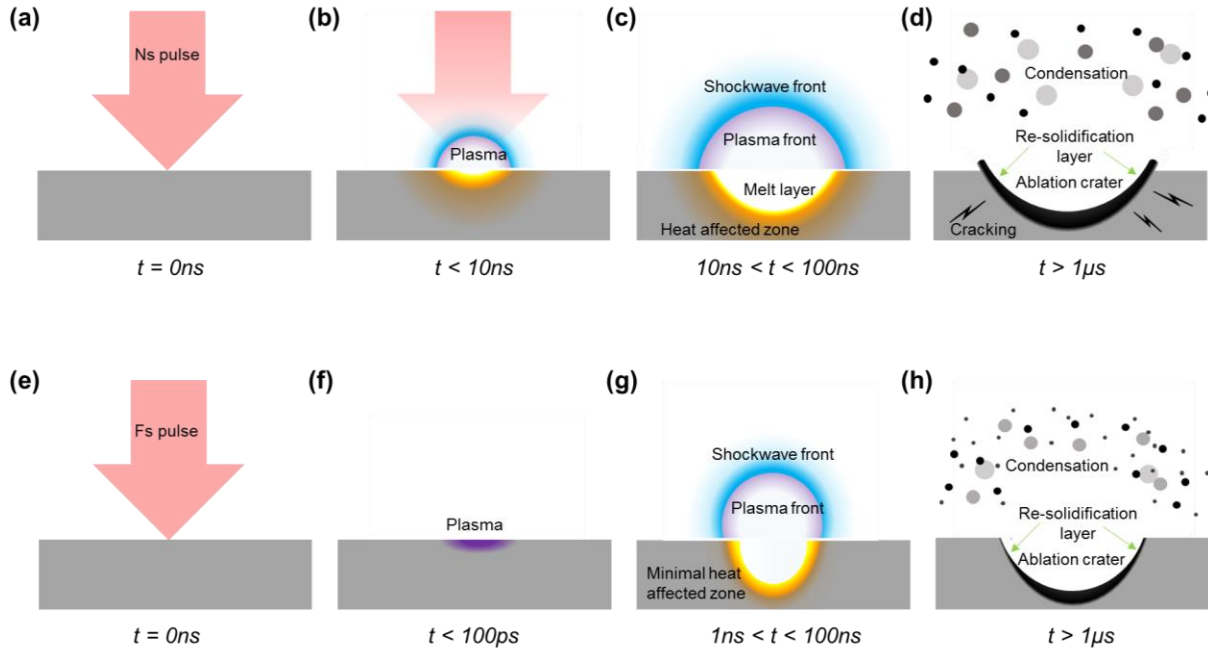


Figure 6. Cartoon illustrating some of the processes involved in (a) nanosecond and (b) femtosecond laser ablation.

### 2.2.2 Femtosecond Ablation

In fs laser ablation, the duration of the pulse is shorter than the electron cooling time so electrons become ionized and ejected without heating of the lattice. In dielectrics, the remaining positively charged material disintegrates via Coulomb explosion in a few ps. In metals, Coulomb

explosion is inhibited by high electron mobility so thermal processes dominate [38]. For semiconductors, Coulomb explosion is possible with sufficient laser fluence. Energy transfer from the electrons to the lattice via electron-phonon coupling occurs in the next 10-100ps at which point ablation processes can take place [39]. Melting occurs as the temperature increases. High temperatures at the surface generate thermos-elastic stresses that can generate voids below a spallation layer and phase explosion with sufficient fluence. Phase explosion can result in droplets around the crater with a variety of sizes. Material is also ejected around this time via thermal processes such as thermal vaporization [30]. A shock wave from the expanding plasma plume can also ablate more material [11]. Additional residual thermal energy can be generated from re-deposition of the ablated material by the laser-air plasma [40]. The laser does not interact with the plasma plume after it is initially absorbed so there is no plasma shielding.

Since the energy is deposited in a time much shorter than the electron cooling time, the electrons and the lattice are in a state of non-equilibrium ( $T_e \neq T$ ) and the temperature is described by a two temperature model [32, 33, 30]:

$$q_e(T_e)c_e(T_e)\frac{\partial T(x,t)}{\partial t} = \frac{\partial}{\partial x} \left[ k_e(T_e, T) \frac{\partial T(x,t)}{\partial x} \right] - \Gamma_{e-p}(T_e - T) + \alpha I(x,t) \quad (2.5)$$

and

$$q_p(T)c_p(T)\frac{\partial T(x,t)}{\partial t} = \frac{\partial}{\partial x} \left[ k_l(T) \frac{\partial T(x,t)}{\partial x} \right] - \Gamma_{e-p}(T_e - T) \quad (2.6)$$

where  $k_e$  is the non-equilibrium thermal electron conductivity,  $k_l$  is the thermal conductivity of the lattice, and  $q_e$ ,  $c_e$ , and  $q_p$ ,  $c_p$  denote the mass density and specific heat of the electrons and the

lattice, respectively.  $\Gamma_{e-p}$  is an expression for the electron-phonon coupling constant. Solutions to these coupled equations can only be solved numerically.

Additional processes of material removal during fs ablation can occur at later times. A second ablation step occurring after 30-50ns has been reported in metals [41]. It is suggested that ablation here is a result of longer thermal processes such as boiling after heterogeneous or homogeneous nucleation [41]. Multiple stress waves in the material have also been reported to occur on this timescale in glass [42]. The relevant processes involved and their timescales depend on the material and fluence of the laser, which result in different crater shapes and features.

### 2.2.3 Double-Pulse Ablation

#### 2.2.3.1 Ns/ns ablation

In double ns pulse experiments, the ablated volume is enhanced compared to a single pulse of the same energy [12]. Krstulovic *et al* found that the ablated volume of titanium in vacuum with 1064nm 4 and 5ns pulses at 210 and 40mJ increased for pulse delays up to 370ns where they saw maximum enhancement [34]. The ablation was enhanced for delays up to 370ns as consequence of decreased ablation threshold and decreased reflectivity by thermal effects. The enhancement factor was less for delays shorter than 370ns because the second pulse was shielded by plasma produced by the first pulse. Optimal delay thus requires balancing screening effects with thermal effects leading to decreased ablation threshold. On the other hand, absorption of the second pulse by the plasma can also enhance ablation. When the second pulse is absorbed by the material ejected by the first pulse, thermal conduction efficiently transports energy from the plasma to the surface that can lead to additional mass removal [43]. Alternatively, absorption of the second pulse by the

ejecta can enhance absorption by energizing the ejecta sufficiently to inhibit re-deposition of the ablated particles inside the ablation hole. Another study found enhancements in drilling of stainless steel using 532nm double pulses with delays between 30 and 150ns at fluences between 20-200J/cm<sup>2</sup> [43]. The dominating enhancement mechanisms depend on the energy and wavelength of the pulse, the target material, and the ambient pressure.

#### *2.2.3.2 Fs/fs ablation*

In double fs pulse experiments, inter-pulse delays below 1ps yield the same ablation depths as a single pulse of equivalent energy since this time delay is less than the time for electron thermalization [44]. Delays between 10-100ps have reduced ablation compared to a single fs pulse, which is attributed to interaction of the second pulse with plume [44]. Ablation enhancement is finally seen after delays of 100's of ps [44]. In high rep rate experiments, the ablation rate improves with the number of pulses, which is attributed to incubation effects and lowered ablation threshold. Incubation effects arise from increased number of defects after ablation and lowered ablation thresholds arise from changes in the optical and thermal properties of the material. A number of processes on a variety of timescales lead to ablation and it is critical to optimize the timing of the pulses for maximal ablation rates.

#### *2.2.3.3 Fs/ns ablation*

Superimposing fs and ns pulses can increase the total amount of ablated material compared to either pulse alone. Two experiments that investigated ablation with dual fs-ns pulses with inter-pulse delays in the nanosecond regime observed ablation enhancement. Thereberge and Chin *et al* used a 130fs pulse at 800nm followed by a 10ns pulse at 532nm with respective fluences of 70 and



4.5-30J/cm<sup>2</sup>. They found the maximum ablated volume of fused silica occurred with a 30ns inter-pulse delay, even when the fluence of ns pulse was below the damage threshold [45]. Possible reasons for increased ablation were thought to be increased absorption of the ns pulse by electrons excited to the conduction band by the fs pulse, increased defects and Frenkel pairs that are more easily excited by the ns pulse, and reduced plasma shielding. This delay corresponded to a dip in the plasma density of the ejected plume suggesting screening of the ns pulse by the plasma was minimized. Another explanation that was not mentioned could be coupling of the ns pulse to ejecta that follow the quickly expanding plasma plume [46]. A similar experiment with fused silica noted different results as maximum ablation occurred with 0 ns inter-pulse delay for set of five dual-pulses at 120fs, 800nm, and 3.8J/cm<sup>2</sup> and 30ns, 355nm, and 5.6J/cm<sup>2</sup> for the fs and ns pulses [47]. Little explanation for the enhancement was provided. There is significant evidence that a dual-pulse fs-ns configuration can lead to enhanced ablation rates. Furthermore, there are many possible mechanisms for enhancement that can be most efficiently utilized by optimizing the inter-pulse delay. A thorough investigation of dual-pulse fs-ns ablation is needed.

## CHAPTER 3: FACILITIES AND EXPERIMENTAL DETAILS

### 3.1 Lasers

#### 3.1.1 Femtosecond Laser Source

The femtosecond source in this experiment was provided by the Multi-Terawatt Femtosecond Laser (MTFL) designed and assembled at the Laser Plasma Laboratory at the University of Central Florida. MTFL achieves short, high power pulses by chirped pulse amplification (CPA). The system is seeded by 35fs pulses centered at 800nm at a rate of 73MHz generated by a Titanium:Sapphire (Ti:Sapph) based oscillator (Spectra-Physics Tsunami) pumped by CW 532nm laser at (Spectra-Physics Millennia V) and mode-locked with Kerr passive mode-locking and an acousto-optic modulator (AOM). The peak power is reduced before amplification by stretching the pulse to 450ps with a Martinez grating stretcher. Optimal dispersion for pulse compression is added to the seed by a acousto-optic programmable dispersive filter (AOPDF) (Fastlite DAZZLER) before it is sent to the first amplifier, a Ti:Sapph based Z-shaped cavity pumped by a 20W laser at 527nm at 1kHz (Spectra-Physics Evolution). After ~40 round trips in the regenerative amplifier, two Pockels cells and a pulse picker let a 1.3mJ pulse through to the pre-amplifier at a rate of 10Hz. The pre-amplifier is a Ti:Sapph based bow-tie shaped cavity pumped at 10Hz with 700mJ pulses at 532nm (Spectra-Physics Quanta-Ray Pro 290). After three passes, the pulse has an energy 130mJ where it then passes through a light valve, allowing continuous control of the pulse energy from 0-40mJ at the output. Alternatively, the pulse is sent to the final amplifier. The pulses reach 500mJ after 2 passes in the final amplifier, a Ti:Sapph bowtie-shaped cavity pumped by 2J pulses at 532nm (Continuum Powerlite DLS). Finally, a

Treacy grating compressor compresses the output from the pre-amplifier or final amplifier down to 35fs [48]. MTFL yields a final output of 35fs pulses centered at 800nm at 10Hz with energies of 0-60mJ (pre-amplifier line) or 250mJ (final amplifier line). The output is p-polarized. In this work, the experiments were performed using 4-5mJ pulses from the pre-amplifier. At this energy, the pulse has a 15% shot-to-shot stability and 3% RMS stability.

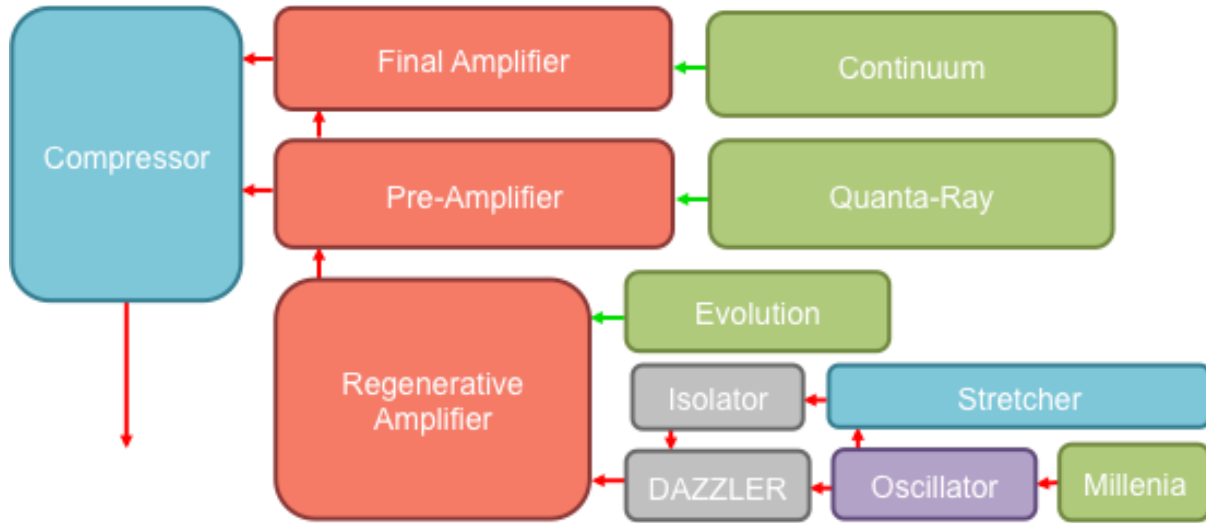


Figure 7. Simplified schematic of MTFL.

### 3.1.2 Nanosecond Laser Source

Nanosecond pulses were provided by a Quantel CFR200. The Quantel is a compact commercial Nd:YAG laser that outputs 240mJ pulses centered at 1064nm with 8ns pulse duration at a rate of 10Hz. The output is elliptically polarized. Continuous control of the energy from 4-22mJ was achieved with a light valve at the output consisting of a half-wave plate and polarization dependent 90/10 beam splitter. After these components the beam was linearly polarized. At this output, the Quantel has 1.5% peak-to-peak stability.

### 3.2 Experimental Set-Up

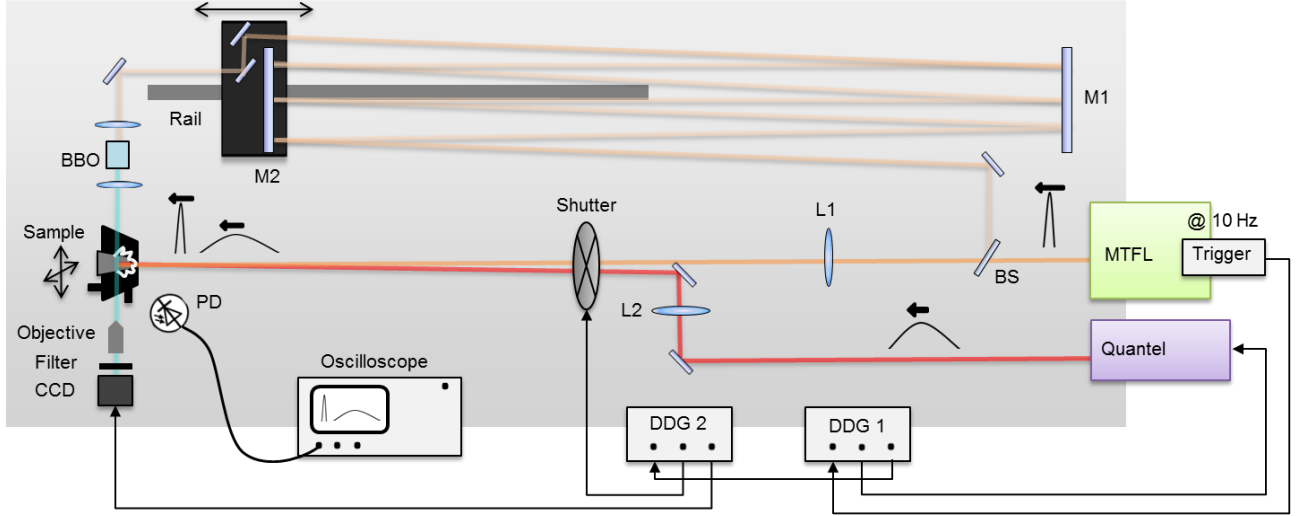
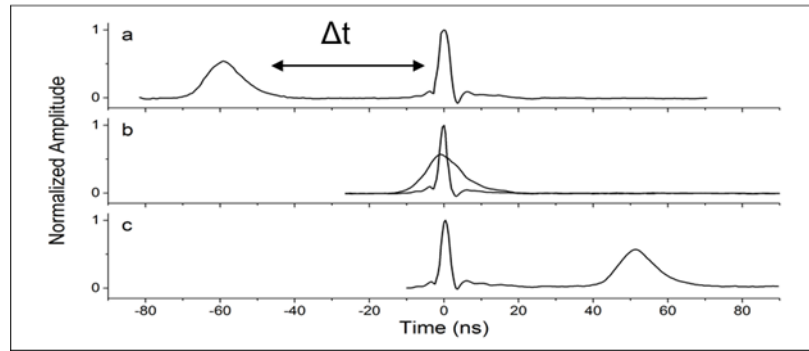


Figure 8. Schematic of experimental set-up.

A schematic of the experimental set-up is shown in Figure 8. In this set-up, the outputs from MTFL and the Quantel are directed to the optical table where the sample is located. The fs output is split by a 90/10 beam splitter for an fs pump and probe beam. The fs pump is focused onto the sample by a 1.5m lens (L1). The ns pump is focused by 1m lens (L2) just before it is combined with fs pump at a shallow angle. Due to the long distance to the sample ( $\sim 1\text{m}$  from the combining mirror), the angle is negligible making the pulses approximately collinear. Both pumps then pass through a triggered electronically-driven shutter for single-shot ablation on the target.

To control the temporal spacing of the pulses, the Quantel is externally triggered off MTFL with a digital delay generator (DDG) (Stanford Research Systems DG645, DDG 1 in Figure 8). A Germanium fast photodiode connected to a 500MHz oscilloscope (Tektronix DPO 3054) is used to monitor the timing of the pulses. Although the fast photodiode and oscilloscope cannot resolve any details of the fs pulse, the uncertainty in the temporal location of the fs peak is within the

temporal resolution provided by the oscilloscope. After optimizing the delay between MTFL and the Quantel with the DDG such that the pulse peaks are overlapped in time, the delay is increased or decreased with the DDG to change the delay between the pulses. Using the fs pulse as a reference for  $t=0$ , a negative inter-pulse delay  $\Delta t$  corresponds to the ns pulse arriving before the fs pulse and a positive  $\Delta t$  corresponds to the fs pulse arriving first. Oscilloscope traces for select inter-pulse delays are shown in Figure 9.



*Figure 9. Oscilloscope traces of fs-ns dual pulses.*

To investigate single shot ablation, an electrically-driven shutter is also triggered by a DDG synchronized with the lasers (Stanford Research Systems DG535, DDG 2 in Figure 8). The timing of the shutter is set so that only one pulse from each laser passes through to the target while it is open and remains closed long enough to manually block the beams before another shot is let through.

The sample is placed at the focus of each beam, which are directed to the same spot, to maximize the fluence. The GaAs samples are set up on an XY stage normal to the incident beams. Translating the XY stage between shots allows each laser pulse or pulse doublet to interact with a clean part of the sample without needing to remove or replace the sample.

The beam profiles for the fs and ns beams at the focus are shown in Figure 10. The ns beam is focused by a 1m lens for an NA of  $\sim 0.02$  yielding a spot size of  $\sim .006\text{mm}^2$  and the fs beam is focused by a 1.5m lens for an NA of  $\sim 0.01$  yielding a spot size of  $\sim .02\text{mm}^2$ . A 1.5m lens was chosen to focus the fs beam to yield an NA not far from the transition to the non-linear regime (see Ch.1.2), while maintaining consistent beam pointing at the focus. Inconsistent beam pointing can occur during filamentation with hotspots in the beam. At the sample, the fs beam had an intensity of  $\sim 10^{14}\text{W/cm}^2$  and spot diameter of  $150\mu\text{m}$ , which are the same as in a single filament.

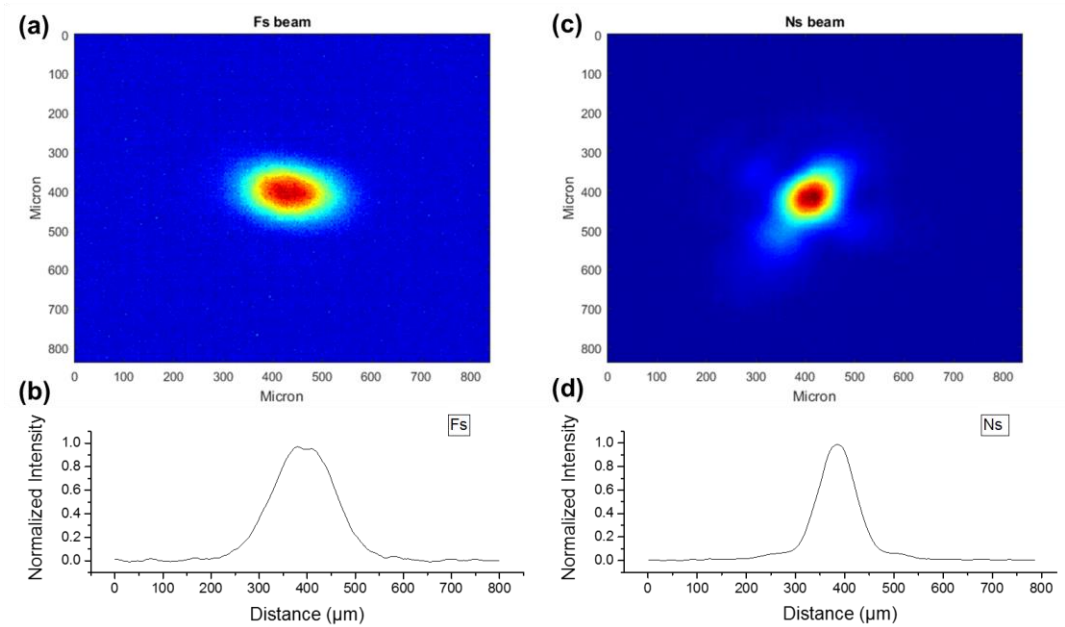


*Figure 10. Beam profiles of the fs (a) and ns (c) beams at focus and lineouts showing their respective normalized intensity profiles (b and d).*

The low-energy probe is picked off from the MTFL line by a 90/10 beam splitter for imaging the plasma and shockwave generated during ablation. The timing of the probe can be adjusted from 0 to 57ns relative to the fs pump, which is roughly controlled by the number of passes between two large silver mirrors (M1 and M2 in Figure 8) as well as the distance between

them. Finer temporal control is obtained by an additional delay line (not shown in Figure 8 for simplicity). The probe is focused into a barium borate (BBO) crystal for second harmonic generation and recollimated before it passes above the target through the generated plasma, perpendicularly to the pump beams, onto a charge coupled device (CCD) (Imaging Source DMK 23UP031). A 10x objective magnifies the image of the plasma on the camera and a blue glass filter (BG12) blocks light from the pump beams and plasma emission. The camera is synchronized with the shutter and triggered by the DDG. A silicon fast photodiode is used to verify the timing of the probe relative to the fs pump.

### **3.3 Samples/Targets**

Polished un-doped S-I GaAs (1 0 0) wafers (MTI Corporation) were used as the target. Semiconductor wafers have a high degree of surface flatness compared to most bulk metals making GaAs ideal for single-shot ablation crater characterization [9]. Additionally, GaAs grows an oxide layer relatively slowly, meaning no extra sample preparation was required to remove the oxide layer [49]. The samples were simply cleaned by blowing them with nitrogen air immediately before ablation. Additionally, the interaction of fs laser pulses with GaAs has been investigated in previous studies [50]. Table 1 summarizes important thermal and optical properties of crystalline un-doped GaAs.

*Table 1. Optical and thermal properties of GaAs at room temperature.*

<u>Property</u>	<u>Value</u>
Refractive index (800nm, 1064nm)	3.68 [51], 3.47 [52]
Absorption coefficient (800nm, 1064nm)	13980cm <sup>-1</sup> [51], 1261cm <sup>-1</sup> [53]
Reflectivity (800nm, 1064nm)	0.33, 0.31 [52]
Band gap	1.424eV or 870.7nm [54]
Ablation threshold at 800nm, 100fs pulses	175mJ/cm <sup>2</sup> [55]
Ablation threshold at 1.35eV, 28ns pulses	~500mJ/cm <sup>2</sup> [56]
Thermal conductivity	0.55W/(cm*K) [54]
Specific heat	0.327J/(g*K) [54]
Crystal density	5.317 g/cm <sup>3</sup> [54]

### **3.4 Diagnostics**

#### **3.4.1 Laser Diagnostics**

To fully characterize the laser pulses interacting with the target several diagnostic techniques are used to measure energy per pulse, pulse duration, and beam profile. An energy meter (Gentec) measures the energy per pulse of both the ns and fs pulses. A Ge fast photodiode with a 500GHz oscilloscope is used to measure the duration of the ns pulse while a FROG technique (Swamp Optics Grenoullie) is used to measure the duration of the fs pulse. Intensity profiles of the ns and fs beams at the focus are determined with a Limaging system [20, 57]. A Limaging system captures the intensity profiles of high intensity beams by propagating the image of the beam through a series of shallow angle wedges to cut down the pulse energy before a CCD.



The intensity profiles are shown in Figure 10. The energy, pulse duration, and intensity distribution in each beam are critical to fully understanding the laser material interaction.

### 3.4.2 Sample Metrology

Sample metrology is performed to determine the size of the ablation crater, surface features, and volume of material ablated. Surface profilometry examining the size and depth of the craters is conducted with scanning white light and optical phase shifting interferometry (Zygo NewView 6300). The Zygo surface profiler reflects light of different wavelengths off the sample surface and a reference mirror and uses the optical phase differences to obtain the depth of the sample. From the Zygo surface data, the volume removed is calculated from the depth at each point in the crater and pixel area of each point. Additional surface features are examined with optical microscopy, revealing more details about the ablation mechanisms. These results are analyzed as a function of inter-pulse delay and compared to single ns and single fs cases.

### 3.4.3 Shadowgraphy

A shadowgraph technique can be used to determine the energy coupled to the sample during ablation [41, 25]. When light propagates through a medium of varying refractive index, the light rays bend as a result of refraction where there is an index gradient. A shadow is left where the light would have propagated, and the regions where the deflected ray hits the detecting plane are brighter. The resulting shadowgraph can thus be used to detect changes in refractive index, which depends on the density of the fluid. Figure 11 shows a simple illustration of the technique. Shadowgraphy is a useful technique for imaging shockwaves. A region of compressed air forms

during shockwave propagation that can clearly be seen by a shadowgraph and shows the front of the shockwave.

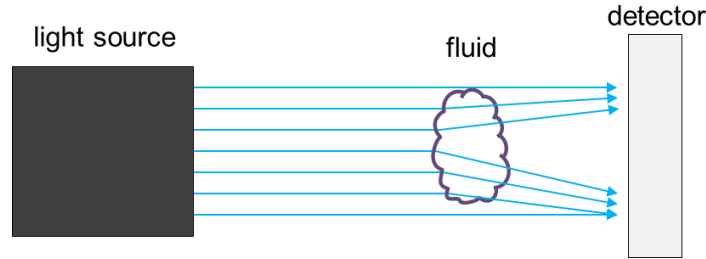


*Figure 11. Simplified illustration of shadowgraphic imaging.*

In this set-up, imaging optics direct the probe into a CCD. A frequency doubled pick-off from MTFLL used as a probe provides an ultra-fast shutter for the camera and fine temporal resolution of the shockwave expansion. The probe is delayed up to 57ns after the fs pump. After imaging the plasma at several delays, analysis of the expanding plasma is used to reveal the dynamics of the ablation processes. These images reveal whether the second pulse interacts with the plasma created by the first pulse or sample itself. Additionally, Sedov-Taylor analysis of the shockwave from the expansion of the plasma plume provides insight on the energy coupling to the sample or plasma as well as the relevant ablation processes.

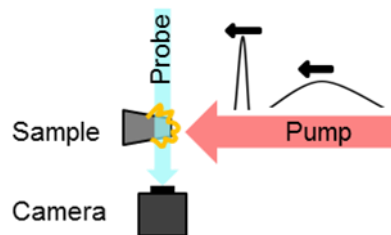


*Figure 12. Schematic of the shadowgraphy technique with the pump-probe setup.*

## CHAPTER 4: ABLATION WITH FS-NS DUAL PULSES

### 4.1 Experimental Results

In this experiment, dual pulse fs-ns ablation was investigated for various inter-pulse delays ranging from -50ns to +1 $\mu$ s. The inter-pulse delays are defined relative to fs pulse, with a positive delay corresponding to the fs pulse preceding the ns pulse (see Figure 9). For these delays, the size of the ablation craters and surface features were analyzed to determine the delays leading to the largest enhancement in material removal and the possible mechanisms of enhancement. Shadowgraphy of the expanding plasma was conducted for several delays between -40ns and +40ns to further investigate the mechanisms of fs-ns dual-pulse ablation. Ablation by a single ns and single fs pulse were also investigated for reference.

#### 4.1.1 Sample Metrology

In this experiment, the size and depth of the ablation craters on GaAs were measured for delays ranging from -50ns to 1 $\mu$ s using the Zygo interferometric microscope. Additional surface features were analyzed through optical microscopy. The energy of the fs pulse was 4.2mJ yielding an intensity of  $\sim 10^{14}$ W/cm<sup>2</sup> (approximately the same intensity as in a single filament) with a .02mm<sup>2</sup> spot size while the energy of the ns pulse was 19mJ yielding an intensity of  $\sim 10^{10}$ W/cm<sup>2</sup> with a .006mm<sup>2</sup> spot size. The beam profiles from which the spot sizes were calculated from are shown in Figure 10. The spot sizes were calculated from the FWHM of the intensity lineouts, which were 150 and 90 $\mu$ m for the fs and ns beams. Approximately 10 shots were taken per delay to obtain an average volume measurement.

#### *4.1.1.1 Zygo results*

The resulting ablation craters were scanned with the Zygo to determine their size and depth. The volume of ablated material was calculated from the Zygo data by multiplying the depth at each point below the un-ablated surface by the area of a pixel. The ablated volume as function of inter-pulse delay is plotted in Figure 13. From the data, significant enhancement in material removal is observed when the fs pulse is followed by the ns pulse. Enhancements greater than 2.5x the volume of a single fs pulse are seen for delays between +40 and +200ns, with the greatest enhancement of 2.7x occurring at +100ns delay. The crater volume decreases for delays beyond 200ns, as shown in Figure 13(b). The ablated volume also decreases significantly for delays at or below 5ns, when the ns pulse is near or followed by the fs pulse, as well as for extremely long delays (experimentally  $\pm 30$ s which is approximately infinity relative to the temporal region of interest). In the latter case, the inter-pulse delays are long enough such that any residual thermal or plasma processes have ended and the total ablated volume approaches the sum of the volumes ablated by the single fs pulse and single ns pulse, shown in pink in Figure 13.

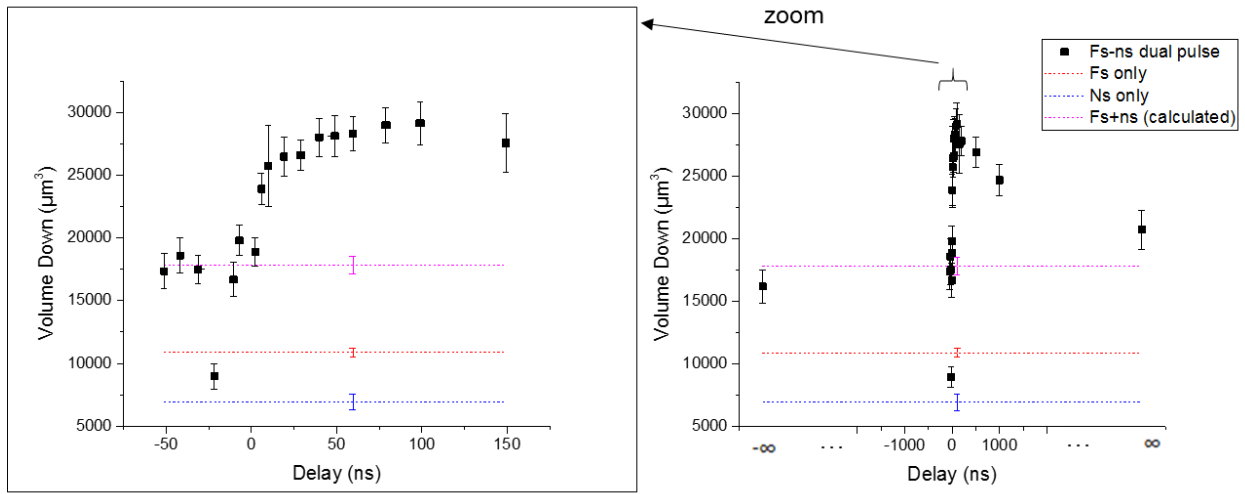


Figure 13. Volume of the ablation crater as function of inter-pulse delay (black squares). The red and blue dotted lines represent the volumes removed by a single fs pulse and single ns pulse (not a function of delay). The pink dotted line is the calculated sum the single fs and single ns volumes. The data is shown on a zoomed in (a) and a zoomed out (b) timescale.

Sample shots of the crater metrology associated with the volume data in Figure 13 measured by the Zygo is shown for the three cases of (i) the fs pulse alone, (ii) ns pulse alone, and (iii) the dual-pulse configuration with each inter-pulse delay in Figure 14. In the cases of the fs pulse alone and ns pulse alone, the ablation craters take on the shape of the beam profiles shown in Fig 14. The fs crater, which has approximately twice as much volume as the ns crater, is wider and shallower. Lineouts of the crater profiles shown in Figure 15 reveal that the fs pulse has a clean ablation while the ns pulse has many peaks and troughs. These properties are characteristics of the fs and ns ablation processes, which involve a more localized deposition of energy and slower hydrodynamic processes with thermal stresses, respectively [32].

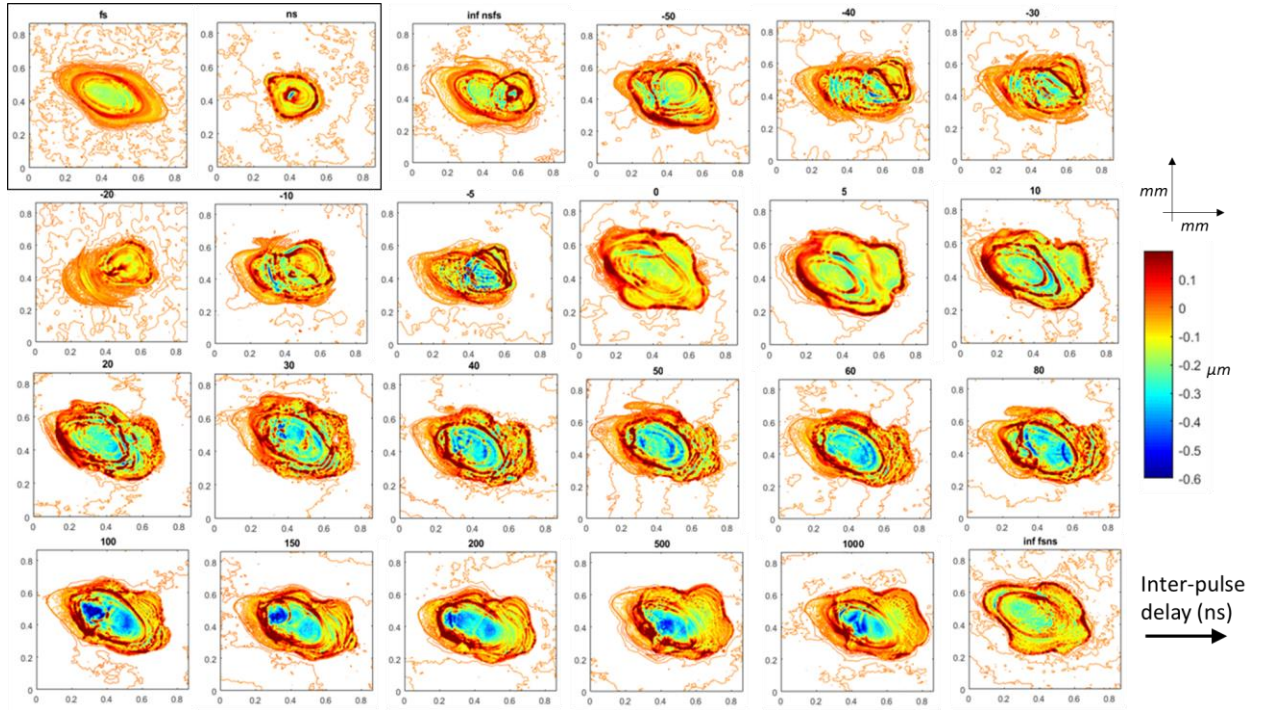
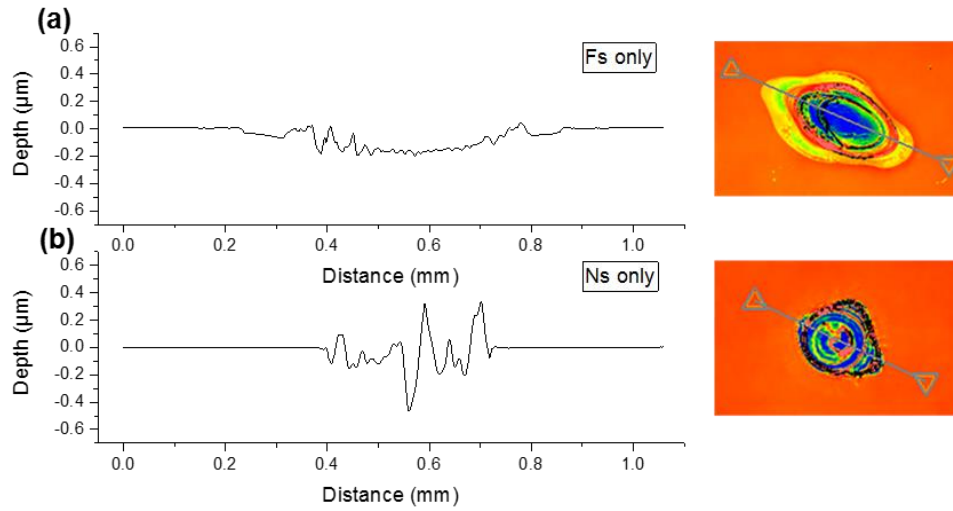


Figure 14. Sample crater profiles showing size and depth for different inter-pulse delays. The delay in ns is given in bold above the profile. The profiles in the black box (top-left) are from a single fs and single ns pulse.

The metrology of the craters produced by fs-ns dual pulses is highly dependent on inter-pulse delay. The inter-pulse delays yielding the most material removal (between +40 and +200ns) are characterized by large depths in region of the fs pulse and the region of overlap between the fs and ns spots. The peak depths for these temporal delays are  $\sim 3\times$  greater than the depth of the crater generated by the fs pulse alone. In the case of the ns pulse preceding the fs pulse, i.e. the case of no significant ablation enhancement, the profiles show two distinguishable craters with depths comparable those of the craters produced by single fs and ns pulses. The crater profiles reveal that in the case of negative delays (ns pulse before the fs pulse), residual processes from the interaction of the ns pulse with the sample had an insignificant effect on the ablation by the fs pulse. When the fs pulse precedes the ns pulse, however, the interaction of the ns pulse with the sample is

strongly affected by the prior fs pulse-material interaction. Since positive delays lead to more material removal, it follows that the mechanisms leading to enhanced ablation are a result of these interactions.



*Figure 15. Lineouts across the craters generated by a single fs (a) and single ns (b) pulse. The pictures on the right indicate where the lineouts were taken.*

Lineouts of the crater profiles further reveal differences in the ablation processes involved for different inter-pulse delays. Lineouts across select craters are shown in Figure 16. For negative inter-pulse delays, when the fs pulse follows the ns pulse, the lineouts are characterized by high peaks and troughs. This structure with many peaks implies the ablation is dominated by the hydrodynamic eruptions characteristic of ns ablation. When there is zero delay between the pulses, the lineout is shallow and similar to the fs only case. The shallow, smooth profile could be a result of the increased local electrical conductivity from the fs pulse while ns pulse is interacting with the sample. The free electrons generated by the fs pulse interaction with the material would increase the electrical and, subsequently, thermal conductivity of the interaction zone [58].

Increased thermal conductivity causes even distribution of the bed of molten material, inhibiting hydrodynamic instabilities that lead to many peaks and troughs. The positive inter-pulse delays corresponding to the greatest ablation enhancements yielded craters with structures that do not exhibit the dominant traits of either single pulse crater. The craters in this case are deep without large peaks. The enhancement in total ablated volume stems from a combination of deepening the crater while inhibiting the formation of peaks and ridges, which implies the dominant ablation mechanisms must involve the interaction of second pulse with the effects of the first pulse.

The Zygo analysis of the craters uncovers significant differences in the ablation by fs-ns dual-pulses of different inter-pulse delays. The analysis reveals that the negative delays, corresponding to the ns pulse hitting prior to the fs pulse, lead to minimal enhancement of the ablated volume. The craters consisted of high peaks and troughs with depths comparable to the depths of the craters generated by each pulse individually. Positive delays, on the other hand, particularly between +40 and +200ns, lead to significant enhancement of ablation. At these delays, significantly larger craters were generated by ablative processes that inhibited peaks and produced larger depths. These properties imply the enhanced ablation is not dominated by typical fs or ns ablation processes, but is dominated by the interaction of the ns pulse with the residual effects of preceding fs pulse.



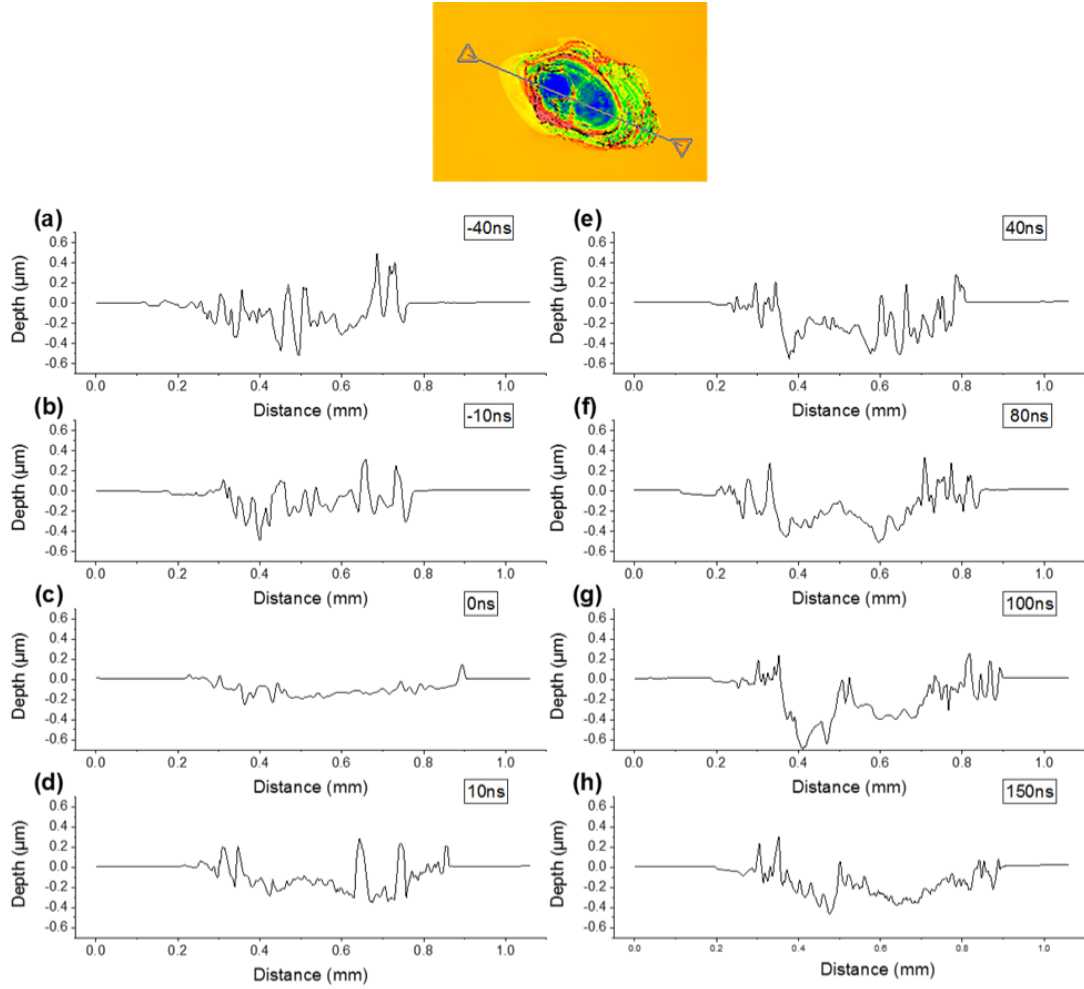
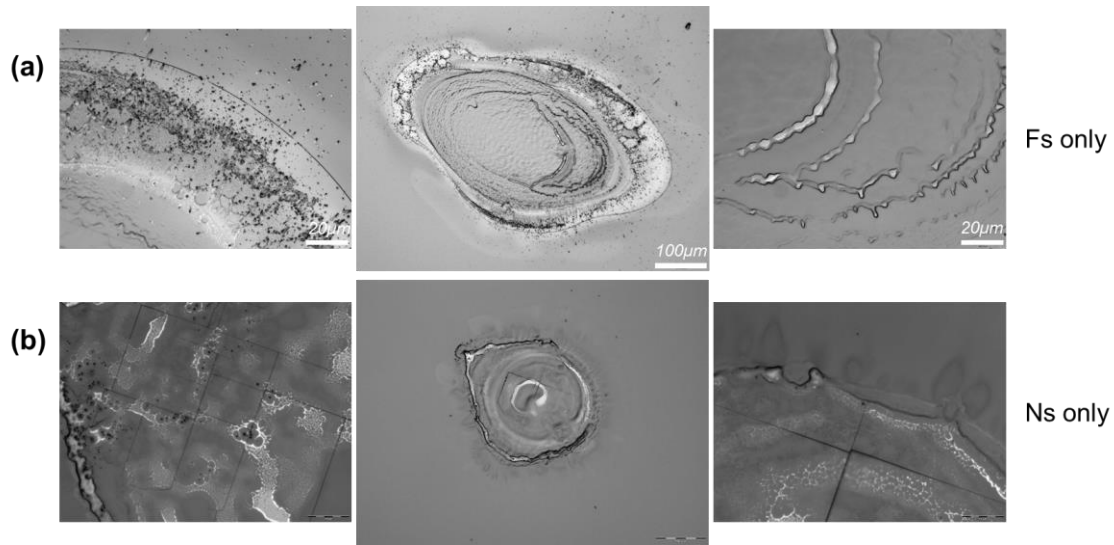


Figure 16. Lineouts across crater profiles for inter-pulse delays of -40ns (a), -10ns(b), 0ns (c), 10ns(d), 40ns(e), 80ns(f), 100ns(g), 150ns(h).

#### 4.1.1.2 Optical microscopy

The craters were also examined with an optical microscope to resolve more surface features. Figure 17 shows microscope images of the craters from a single fs pulse and single ns pulse. The observed features reflect the differences in fs and ns ablation. In Figure 17(a), a smooth crater bottom, distinct crater walls, frozen outward travelling ripples, and large production of nanoparticles indicate material removal dominated by an explosion of plasma [32, 59]. In Figure

17(b), larger gradients at the bottom of the crater, thick crater walls, small voids, surface modification outside the crater, and cracking along the crystal lattice imply material removal via thermal processes such as boiling and thermally induced straining of the material in addition to an explosion of plasma [32, 60, 61]. A combination of these features can be seen in the craters generated by fs-ns dual pulses, with different features being more prominent at different inter-pulse delays. The dominant features imply different ablation mechanisms.



*Figure 17. Optical microscope images of craters generated by single fs (a) and single ns (b) pulses. The images on the far left and far right are zoomed in to show details.*

Microscope images of craters for select inter-pulse delays are shown in Figure 18(a-f). The variety of surface features that appear for different inter-pulse delays are indicative of the various interactions between the pulses with the sample and plasma. The images in the right-most column show changes in texture of the crater surface with changing inter-pulse delay. Negative and short positive delays (a-d) tended to produce surfaces with fractures and rough texture. Craters produced by inter-pulse delays longer than +40ns (e, f), on the other hand, had smooth textures with no obvious cracking. Fracturing of the surface could be indicative of direct interaction of the

fs pulse with sample in negatives delays. The ns pulse transferred heat deep into the material and then the fs pulse, which has a more localized interaction with the sample, rapidly vaporized the top layer, creating stress in the material. Following, the surface quickly cools and condenses, leading to cracking to relieve stress in the material. The fracturing disappears as the inter-pulse delay reaches the regime of significant ablation enhancement, implying different ablation dynamics.

The images on the left-hand side of Figure 18 highlight features on the nano and micro scale. Clusters of nanoparticles and nano- and micro-sized ridge patterns are visible near the edge of the craters produced by negative inter-pulse delays. At 0ns delay, there are significantly less nanoparticles and ridges and a nanoscale folding pattern emerges. The amount of nanoparticles increases after +20ns delay. As the inter-pulse delay increases, changes in the size and distribution of these particles are apparent. These changes are particularly visible in Figure 18(d-f), where particles and droplets with a large size distribution are concentrated near the edge of the crater at +20ns delay, fine particles are distributed throughout the outer part of the crater and beyond at +50ns delay, and larger droplets are seen mostly within the outer region of the crater at +150ns delay. The formation of nanoparticles and droplets typically result from condensation of the plasma and phase explosion. The change in size and location of droplets can thus be explained the ns pulse interacting with the plasma or the sample. For short delays, the plasma generated by the fs pulse is sufficiently dense to absorb the ns pulse. Absorption then energizes and expels the particles in the plasma before they conglomerate and become larger or redeposit on the sample [43, 59]. When the ns pulse comes later, e.g. at +150ns, the expansion of the plasma reduces its density and more of the ns pulse would then interact directly with the molten layer of the sample [34, 60]. A reduced ablation threshold at the molten layer results in better coupling of the pulse to

the sample and larger droplets could expelled as a result of phase explosion [59]. To confirm this hypothesis, a more quantitative analysis of the size, distribution, and composition of the nanoparticles and droplets is needed. Nanoparticles formed through plasma condensation would consist of either Ga or As, as the GaAs molecule separates in the plasma state [29]. Droplets ejected from the molten layer, conversely, would still consist of GaAs molecules. This investigation could be accomplished with a combination of scanning electron microscopy (SEM) and energy-dispersive X-ray spectroscopy (EDS).

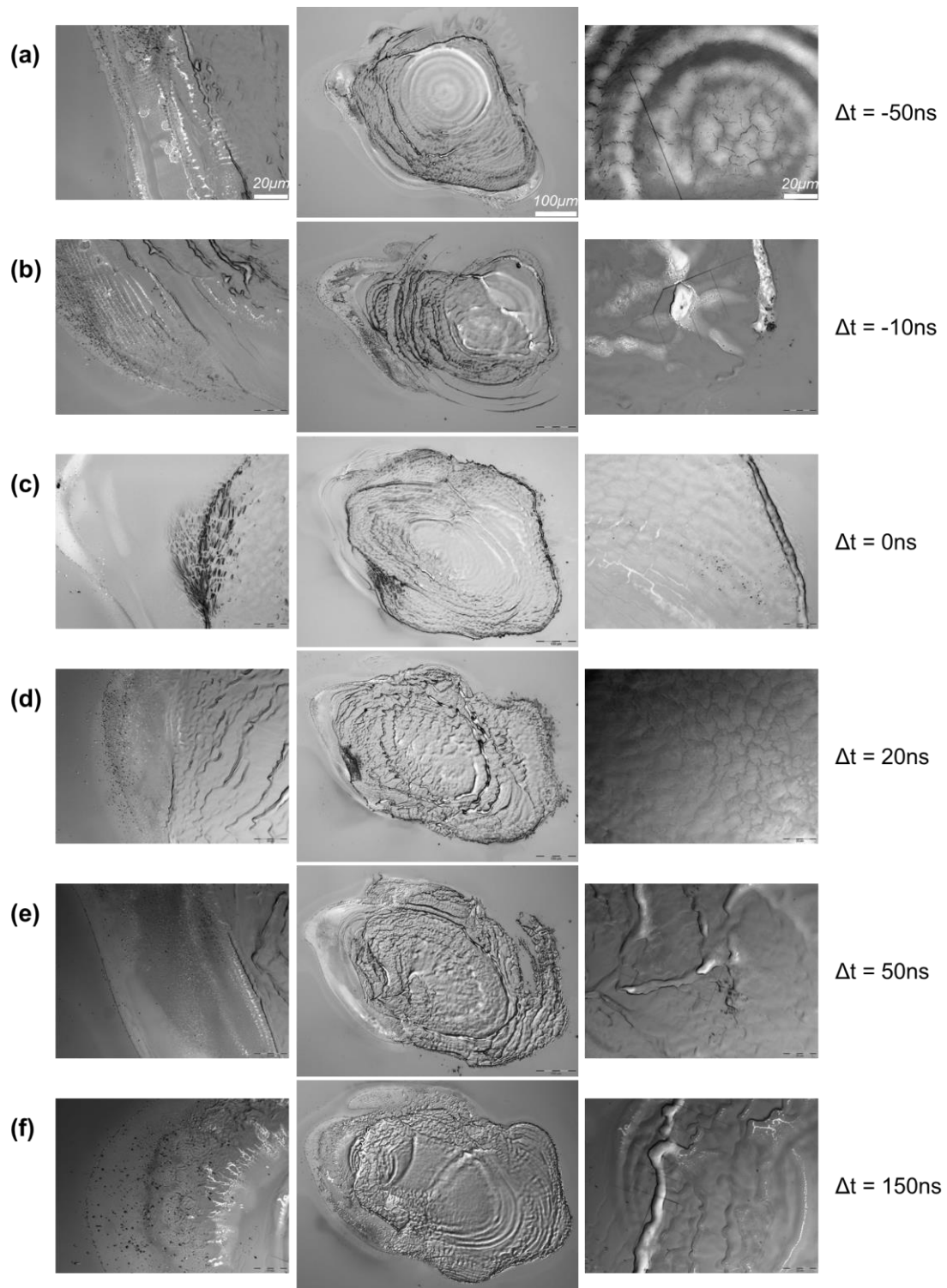
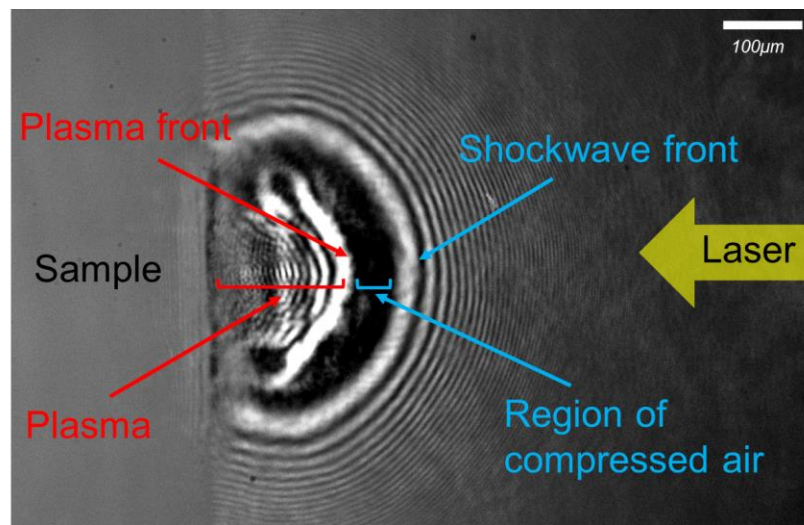


Figure 18. Optical microscope images of craters generated by different inter-pulse delays (a-f). The images on the far left and far right are zoomed in to show detail. The text on the far right indicates the inter-pulse delay.

#### 4.1.2 Shadowgraphy

To learn more about the dynamics involved in ablation, shadowgraphy of the expanding shockwave was done for select inter-pulse delays: -40ns, -20ns, -10ns, 0ns, +10ns, +20ns, and +40ns. The energies of the pulses were lowered slightly to 3.9mJ per pulse for the fs beam and 15mJ per pulse for the ns beam. The energy was lowered slightly to prevent camera saturation and to produce clearer images. The shadowgraph images reveal the evolution of the expanding plasma and shockwave. The explosion takes on a structure consisting of a shock front, a region of compressed air, a plasma front, and a region of plasma. The different regions are illustrated in Figure 19.



*Figure 19. Diagram showing the regions of the expanding plasma and shockwave.*

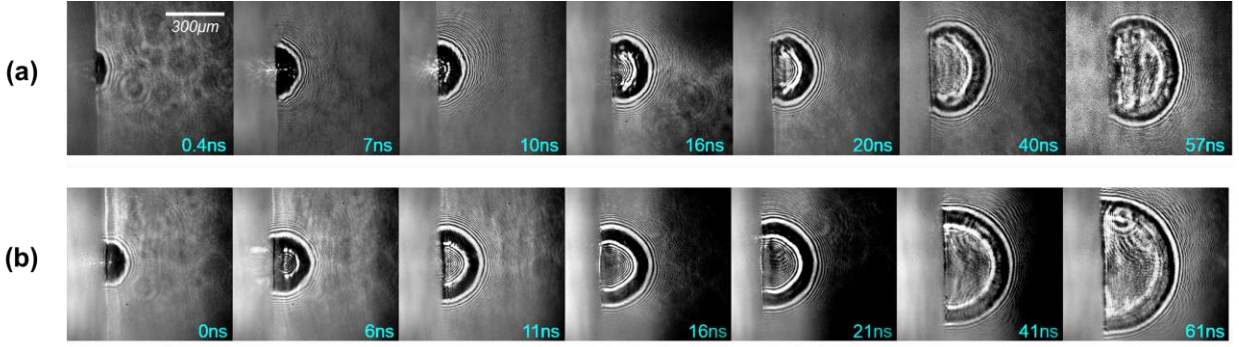


Figure 20. Select shadowgraph images of the expanding shockwave and plasma for single fs (a) and single ns (b) pulses.

Shadowgraph images of the shockwave generated by a single fs and single ns pulse at select probe delays are shown in Figure 20. The images reveal differences in the shape and rate of expansion of the shockwave between the fs and ns cases. The different shapes are a result of the differences in pulse intensities and fs/ns ablation dynamics [60]. The rate of expansion of the shockwave is related to the amount of energy coupling to the sample. In Sedov-Taylor theory, blast wave dynamics can be used to determine the energy of the explosion. The radius  $R$  of the shockwave is related to the energy  $E$  of explosion through [37, 61, 62]:

$$R = \xi \left( \frac{E}{\rho} \right)^{1/5} t^{2/5} \quad (4.1)$$

where  $\xi$  is a ratio of heat capacities equal to 1.033,  $\rho$  is the density of the background air and approximately  $1.2\text{kg/m}^3$ , and  $t$  is time. The shockwave radii as measured from the shadowgraph images are plotted as function of time in Figure 21. Approximately 10 shadowgraph images were taken per probe delay for an average. Also in Figure 21 are fits of Equation 4.1, through which

the shockwave energy was determined. For the fs pulse,  $3.1 \pm 1.2 \text{ mJ}$  of the initial  $3.9 \text{ mJ}$  was coupled while  $3.1 \pm 1.5 \text{ mJ}$  of the initial  $15 \text{ mJ}$  of the ns pulse was coupled.

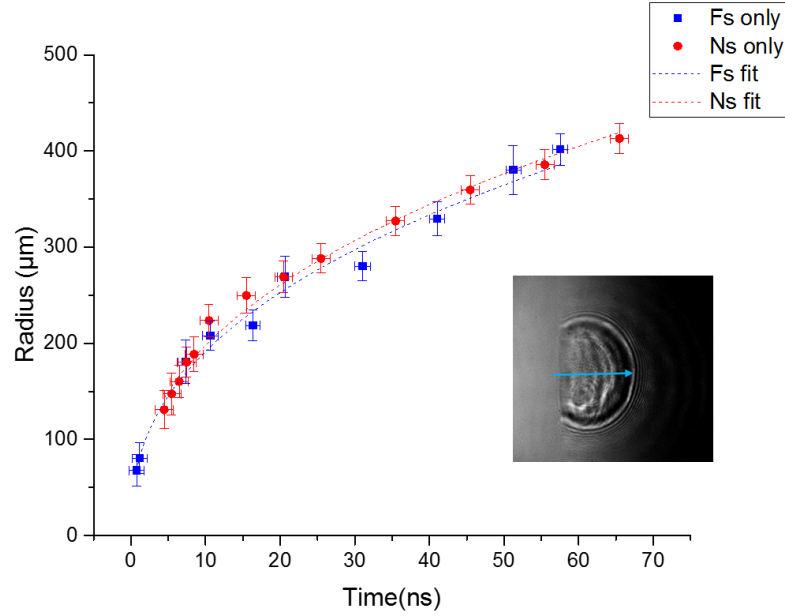


*Figure 21. Longitudinal shockwave radius as a function of time for single fs (blue) and single ns (red) pulses with fits of the Sedov-Taylor equation (blue and red dashed lines.) The image illustrates the measured radius of the shockwave.*

Shadowgraph images of shockwaves from fs–ns dual-pulses are shown in Figure 22. For negative delays (a-c), the fs pulse penetrates the plasma generated by the ns pulse and directly interacts with the sample. At 0 ns delay (d) the pulses interact with the sample at the same time and expand concurrently. For positive delays (e-f), the ns pulse does not penetrate the plasma generated by the fs pulse. Instead, the ns pulse produces a shockwave on the edge of the plasma generated by the fs pulse. This interaction between the ns pulse and plasma is particularly apparent when the ns pulse comes +40 ns after the fs pulse, the inter-pulse delay corresponding to the most removed material for which shadowgraphy was performed. The radii of the shockwave generated



by the ns pulse in this case (Figure 22(f)) are plotted and fit with Equation 4.1 in Figure 23. The image in Figure 23 illustrates how the radii of the shockwave were measured. The expansion of the ns pulse alone is also shown for comparison. Sedov-Taylor analysis reveals the energy in the shockwave produced by the ns pulse increases to  $10 \pm 6 \text{ mJ}$  when the pulse is incident 40ns after the fs pulse. The energy in the shockwave produced by the ns pulse thus increases three-fold with inter-pulse delays of +40ns. Sedov-Taylor analysis was not performed for any other delay combination because the edge of the shockwave due to the second pulse could not be clearly distinguished. Additionally, the changing pressure gradient behind the shockwave produced by the ns pulse complicates the analysis for negative delays.

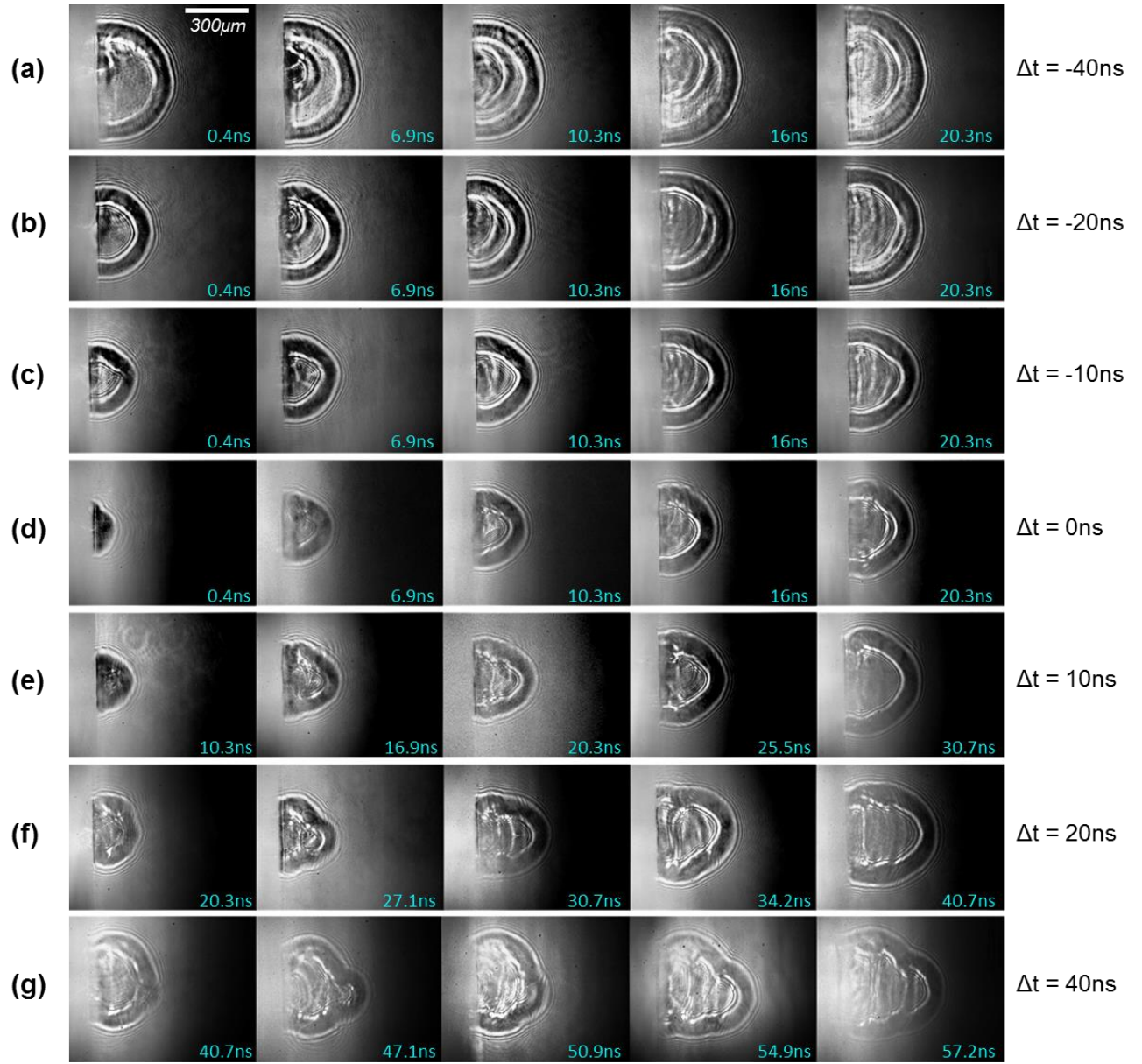


Figure 22. Select shadowgraph images showing the expansion of the shockwave and plasma for inter-pulse delays between -40 and +40 ns (a-g, see text on far right). The timing of the probe (relative to the fs pulse) is given below each image.

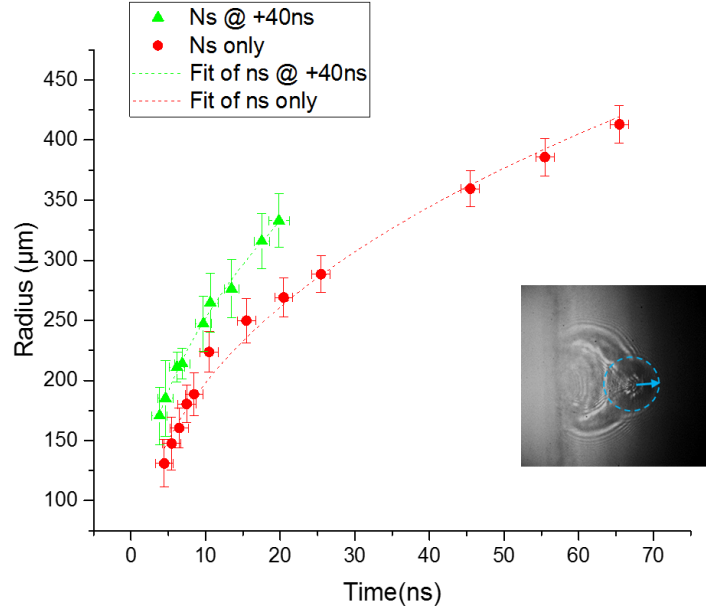


Figure 23. Longitudinal shockwave radius as a function of time for the ns pulse at +40ns inter-pulse delay (green) compared to the single ns pulse (red) with fits of the Sedov-Taylor equation (green and red dashed lines). The image illustrates the measured radius of the shockwave for the delayed ns pulse

Shadowgraphy of dual-pulse ablation reveals significant differences in the plasma dynamics for different inter-pulse delays. For positive temporal delays leading to enhanced ablation, the ns pulse interacts with plasma created by the first pulse and 3x more energy of the ns pulse is coupled. For negative delays where ablation enhancement is minimal, the fs pulse does not interact with the plasma created by the ns pulse. The shadowgraph images indicate that the plasma absorption plays a critical role in enhancing ablation with an ns-fs dual pulse.

## 4.2 Discussion of Ablation Enhancement Mechanisms

The crater profilometry, shadowgraphy of the plasma and shockwave, and Sedov-Taylor analysis reveal enhancements in ablation coincide with strong absorption of the ns pulse by the

plasma produced by the fs pulse. Delays that yielded minimal enhancement, on the other hand, coincided with no visible absorption of the fs pulse by the plasma from the preceding ns pulse. Absorption of laser light by a plasma occurs mainly via Inverse Bremsstrahlung absorption (IBA) and Photoionization (PI) [36]. IBA involves the absorption of light by electrons colliding with ions and neutral atoms. The IBA coefficient is given by [37]:

$$\alpha_{IB} = \sigma_{IB} N_e = \frac{4}{3} \sqrt{\frac{2\pi}{3k_B T_e m_e^3}} \frac{Z^2 e^6}{hc\nu^3} \left(1 - \exp\left(-\frac{h\nu}{k_B T_e}\right)\right) N_e N_i \quad (4.2)$$

where  $\sigma_{IB}$  is the absorption cross-section,  $Z$  is the atomic number,  $k_B$  Boltzmann's constant,  $h$  Planck's constant,  $\nu$  the laser frequency,  $e$  and  $m_e$  the electron charge and mass, and  $N_e$  and  $N_i$  the density of electrons and ions. Photoionization occurs when a photon with energy exceeding the binding energy of an electron to an atom or ion is absorbed and ionizes it. The absorption coefficient of photoionization is approximately [36]:

$$\alpha_{PI} = \sigma_{PI} N_n = \sum_n 2.9 * 10^{-17} \frac{\varepsilon_n^{5/2}}{(h\nu)^3} N_n \quad (4.3)$$

where  $\varepsilon_n$  is the ionization energy and  $N_n$  is the number density of the excited state. The cross section for IBA is larger for plasmas interacting with IR light while PI is more efficient for UV light, so IBA is the dominant mechanism in this case of illumination at 1064nm. No absorption of the fs pulse following the ns pulse (negative inter-pulse delays) is likely a result of the ns pulse generating a less dense plasma due to it having less intensity. Additionally, the fs pulse has a shorter wavelength meaning it has a smaller IBA cross section and larger critical plasma density.

The absorption of the ns pulse by the plasma created by the fs pulse results in enhanced material removal through a number of processes. The dominant process is most likely material expulsion from the pressure of a shockwave propagating towards the material. When the ns pulse is absorbed by the plasma of the fs pulse, it generates a shockwave that propagates into the air and a shockwave that propagates into the plasma towards the sample. The pressure just behind a shockwave in Sedov-Taylor theory is related to the velocity of a shockwave  $D$  by [37]:

$$p = \frac{2}{\gamma + 1} \rho_0 D^2 \quad (4.4)$$

where  $\gamma$  and  $\rho_0$  are the specific heat ratio and density of the background medium. Sedov-Taylor analysis reveals that 3x more energy of the ns pulse went into the shockwave at +40ns inter-pulse delay compared to the ns pulse alone. The increased amount of energy, observed through faster expansion of the plasma, results in higher pressure on the sample. Higher pressure acting on the sample would expel more material, leaving deeper craters as seen in Figures 14, 16, and 18. Additionally, the counter-propagation of the shockwave from the fs pulse expanding into air and the shockwave from the ns pulse propagating into the plasma could have the effect of confining high temperatures above the sample surface and enhance ablation by thermal processes [65].

Another mechanism of material removal could be through heating of the plasma and its constituents with absorption of laser light by the plasma. Ablation can then be enhanced through a number of processes including preventing condensation of the plasma that results in particles being re-deposited on the sample, energizing particles in the plasma and expelling them, or heating particles that efficiently transfer energy to the sample. At longer delays, the ns pulse may interact directly with the sample. Phase explosion is one way more material could be removed in this case.

The different sizes and distributions of the particles with different inter-pulse delays in Figure 18 implies a combination of these processes are occurring. A more detailed and quantitative analysis of the features on the crater surfaces is required to explore which mechanisms are occurring.

## CHAPTER 5: CONCLUSION

This investigation demonstrates enhanced material removal through optimization of the inter-pulse delay of a dual-pulse consisting of an ns pulse and fs pulse in the filamentation intensity regime. Crater profilometry revealed significant enhancements to ablation for inter-pulse delays between +40 and +200ns. These craters were significantly deeper and cleaner than other inter-pulse delays, appearing as though the production of peaks and troughs had been suppressed. Furthermore, shadowgraphy of the shockwaves and plasma for inter-pulse delays between -40 and +40ns revealed strong absorption of the ns pulse by the plasma from the preceding fs pulse at +40ns, the delay yielding the most ablation. The enhanced ablation is determined to be a result of enhanced coupling of the ns pulse to plasma, which could remove material through high shockwave pressures and heating of the plasma. For longer delays, it is suspected that ns pulse interacts more directly with the molten layer of the sample, in which case residual thermal effects from the fs pulse ablation play an important role. While more analysis is required to determine the exact methods of material removal, this work presents a promising method of improving the single-shot ablation rate a high intensity fs pulse by augmenting it with a delayed ns pulse. These results provide a means of enhancing ablation by femtosecond filaments that is critical to advancing long-range laser ablation.

## REFERENCES

- [1] D. Neely, R. Allot, B. Bingham, J. Collier, J. Greenhalgh, M. Michaelis, J. Phillips, C. R. Phipps and P. McKenna, "Energy coupling in short pulse laser solid interactions and its impact for space debris removal," *Optical Society of America*, vol. 53, no. 31, pp. 141-144, 2014.
- [2] W. Wang, X. Mei, G. Jiang, S. Lei and C. Yang, "Effect of two typical focal positions on microstructure shape and morphology in femtosecond laser multi-pulse ablation of metals," *Applied Surface Science*, vol. 255, pp. 2303-2311, 2008.
- [3] J. Cheng, C. Liu, S. Shang, D. Liu, W. D. G. Perrie and K. Watkins, "A review of ultrashort laser materials micromachining," *Optics & Laser Technology*, vol. 46, pp. 88-102, 2013.
- [4] A. Vogel and V. Venugopalan, "Mechanisms of Pulsed Laser Ablation of Biological Tissues," *Chemical Reviews*, vol. 103, pp. 577-644, 2003.
- [5] R. Ganeev, "Laser Cleaning of Art," in *Laser-Surface Interactions*, Dordrecht, Springer, 2014.
- [6] A. Couairon and A. Mysyrowicz, "Femtosecond filamentation in transparent media," *Physics Reports*, vol. 441, no. 2-4, pp. 47-189, 2007.
- [7] M. Durand, A. Houard, B. Prade, A. Mysyrowicz, A. Durecu, B. Moreau, D. Fleury, O. Vasseur, H. Borchert, K. Diener, R. Schmitt, F. Theberge, M. Chateauneuf, J. Daigle and J. Dubois, "Kilometer range filamentation," *Optics Express*, vol. 21, no. 22, pp. 26836-45, 2013.
- [8] A. Valenzuela, C. Munson, A. Porwitzky, W. Matthew and M. Richardson, "Comparison between geometrically focused pulses versus filaments in femtosecond laser ablation of steel and titanium alloys," *Applied Physics B*, vol. 116, no. 2, pp. 485-491, 2014.
- [9] M. Weidman, K. Lim, M. Ramme, M. Durand, M. Baudelet and M. Richardson, "Stand-off filament-induced ablation of gallium arsenide," *Applied Physics Letters*, vol. 101, no. 3, p. 034101, 2012.



- [10] Z. Xu, W. Liu, N. Zhang, M. Wang and X. Zhu, "Effect of intensity clamping on laser ablation by intense femtosecond laser pulses," *Optics Express*, vol. 16, pp. 3604-3609, 2008.
- [11] J. Scaffidi, J. Pearman, C. Carter, B. W. Colstin and S. M. Angel, "Temporal dependence of the enhancement of material removal in femtosecond-nanosecond dual-pulse laser induced breakdown spectroscopy," *Applied Optics*, vol. 43, no. 35, 2004.
- [12] J. Scaffidi, S. M. Angel and D. A. Cremers, "Emission Enhancement Mechanisms in Dual-Pulse LIBS," *Analytical Chemistry*, vol. 78, no. 1, pp. 24-32, 2006.
- [13] W. Liu and S. Chin, "Direct measurement of the critical power of femtosecond Ti:sapphire laser pulse in air," *Optics Express*, vol. 13, no. 15, p. 5750, 2005.
- [14] M. Mlejnek, M. Kolesik, J. Maloney and E. Wright, "Optically turbulent femtosecond light guide in air," *Physical Review Letters*, vol. 83, no. 15, p. 2938–2941, 1999.
- [15] R. Boyd, *Nonlinear Optics*, New York: Academic Press, 2003.
- [16] P. Bejot, J. Kasparian and S. Henin, "Higher-order Kerr terms allow ionization free filamentation in gases," *Physical Review Letters*, vol. 104, p. 103903, 2010.
- [17] Y. E. Geints, A. M. Kabanov, A. A. Zemlyanov, E. E. Bykova and O. A. Bukin, "Kerr-driven nonlinear refractive index of air at 800 and 400nm measured through femtosecond laser pulse filamentation," *Applied Physics Letters*, vol. 99, no. 18, p. 181114, 2011.
- [18] J. H. Marburger, "Self-focusing: theory," *Progress in Quantum Electronics*, vol. 4, pp. 35-110, 1975.
- [19] S. Chin, S. Hosseini, W. Liu, Q. Luo, F. Therberge, N. Akozbek, A. Becker, V. Kandidov, O. Kosareva and H. Schroder, "The propagation of powerful femtosecond laser pulses in optical media: physics, applications, and new challenges," *Canadian Journal of Physics*, vol. 83, no. 9, pp. 863-905, 2005.
- [20] K. Lim, M. Durand, M. Baudelet and M. Richardson, "Transition from linear-to nonlinear-focusing regime in filamentation," *Scientific Reports*, vol. 4, p. 7217, 2014.

- [21] M. Feit and J. and Fleck, "Effect of refraction on spot-size dependence of laser induced breakdown," *Applied Physics Letters*, vol. 24, no. 4, pp. 169-172, 1974.
- [22] W. Liu, F. Thérberge, E. Arévalo, J. F. Gravel, A. Becker and S. L. Chin, "Experiment and simulations on the energy reservoir effect in femtosecond light filaments," *Optics Letters*, vol. 30, no. 19, 2005.
- [23] A. Dergachev, A. Ionin, V. Kandidov, D. Mokrousova, L. Seleznev, D. Sinitsyn, E. Sunchugasheva and S. Shlenov, "The influence of the energy reservoir on the plasma channel in focused femtosecond laser beams," *IOP Science*, vol. 25, no. 065402, 2015.
- [24] S. Eisenmann, J. Peñano, P. Sprangle and A. Zigler, "Effect of an Energy Reservoir on the Atmospheric Propagation of Laser-Plasma Filaments," *Physical Review Letters*, vol. 100, no. 155003, 2008.
- [25] J. Cheonha, D. Harper, K. Lim, M. Durand, M. Chini, M. Baudelet and M. Richardson, "Interaction of a single laser filament with a single water droplet," *Journal of Optics*, vol. 17, no. 5, 2015.
- [26] F. Courvoisier, V. Boutou, J. Kaspiran, E. Salmon, G. Méjean, J. Yu and J.-P. Wolf, "Ultraintense light filaments transmitted through clouds," *Applied Physics Letters*, vol. 83, pp. 213-215, 2003.
- [27] M. Kolesik and J. V. Moloney, "Self-healing femtosecond light filaments," *Optics Letters*, vol. 29, no. 6, 2004.
- [28] I. Grazuleviciute, G. Tamosauska, J. V., A. Couairon, D. Faccio and A. Dubietis, "Self-reconstructing spatiotemporal light bulles," *Optics Express*, vol. 22, no. 25, pp. 30613-30622, 2014.
- [29] M. Weidman and M. Richardson, "Femtosecond Laser Filamentation: Characterization for Spectroscopy Applications," PhD Thesis Dissertation, CREOL, the College of Optics and Photonics at the University of Central Florida, Orlando, FL, 2012.
- [30] D. Bauerle, *Laser Processing and Chemistry (Fourth Edition)*, Springer, 2011.

- [31] B. Rethfeld, K. Sokolowski-Tinten, V. d. Linde, D. and S. Anisimov, "Timescales in the response of materials to femtosecond laser excitation," *Applied Physics A*, vol. 79, pp. 767-769, 2004.
- [32] B. N. Chichkov, C. Momma, S. Nolte, F. von Alvensleben and A. Tunnermann, "Femtosecond, picosecond, and nanosecond laser ablation of solids," *Applied Physics A*, vol. 63, pp. 109-115, 1996.
- [33] G. Ertl, H. Luth and D. L. Mills, "Pulsed Laser Ablation of Solids: Basics, Theory, and Applications," in *Springer Series in Surface Sciences*, Berlin , 53, 2014.
- [34] N. Krstilovic and S. Milosevic, "Drilling enhancement by nanosecond-nanosecond collinear dual-pulse laser ablation of titanium in vacuum," *Applied Surface Science*, vol. 256, pp. 4142-4148, 2010.
- [35] R. Bernath and M. Richardson, "High-intensity ultra-fast laser interaction technologies," PhD Dissertation, CREOL, The College of Optics and Photonics, University of Central Florida, Orlando, FL, 2007.
- [36] M. Allmen and A. Blatter, *Laser-Beam Interactions with Materials: physical principles and applications (Second Edition)*, Berlin: Springer, 1995.
- [37] Y. Zel'dovich and Y. Raizer, *Physics of Shock Waves and High-Temperature Hydrodynamic Phenomena*, Mineola, New York: Dover Publications, 2002.
- [38] N. Bulgakova, R. Soian, A. Rosenfeld, I. Hertel, W. Marine and E. E. B. Campbell, "A general continuum approach to describe fast electronic transport in pulsed laser irradiated materials: The problem of Coulomb explosion," *Applied Physics A*, vol. 81, no. 2, pp. 345-356, 2005.
- [39] J. P. Colombier, P. Combis, A. Rosenfeld, I. V. Hertel, E. Audouard and R. Stoian, "Optimized energy coupling at ultrafast laser-irradiated metal surfaces by tailoring intensity envelopes: Consequences for material removal from Al samples," *Physical Review B*, vol. 74, no. 22, p. 224106, 2006.
- [40] A. Vorobyev and C. Guo, "Enhanced energy coupling in femtosecond laser-metal interactions at high intensities," *Optics Express*, vol. 14, no. 26, p. 13113, 2006.

- [41] J. König, S. Nolte and A. Tunnermann, "Plasma evolution during metal ablation with ultrashort laser pulses," *Optics Express*, vol. 13, no. 26, p. 10597, 2005.
- [42] H. Hu, X. Wang and H. Zhai, "High-fluence femtosecond laser ablation of silica glass: effects of laser induced pressure," *Journal of Physics D: Applied Physics*, vol. 44, no. 135202, 2011.
- [43] A. C. Forsman, P. S. Banks, M. D. Perry, E. M. Campbell, A. L. Dodell and M. S. Armas, "Double-pulse machining as a technique for the enhancement of material removal rates in laser machining of metals," *Journal of Applied Physics*, vol. 98, p. 033302, 2005.
- [44] J. Mildner, C. Sarpe, N. Gotte, M. Wollenhaupt and T. Baumert, "Emission signal enhancement of laser ablation of metals (aluminum and titanium) by time delayed femtosecond double pulses from femtoseconds to nanoseconds," *Applied Surface Science*, vol. 302, pp. 291-298, 2013.
- [45] F. Theberge and S. Chin, "Enhanced ablation of silica by the superposition of femtosecond and nanosecond laser pulses," *Applied Physics A*, vol. 80, pp. 1505-1510, 2005.
- [46] E. Axente, I. N. Mihailescu, J. Hermann and T. Itina, "Probing electron-phonon coupling in metals via observations of ablation plumes produced by two delayed short laser pulses," *Applied Physics Letters*, vol. 99, no. 081502, 2011.
- [47] C.-H. Lin, Z.-H. Rao, L. Jiang, W.-J. Tsai, P.-H. Wu, C.-W. Chien, S.-J. Chen and H.-L. Tsai, "Investigations of femtosecond-nanosecond dual-beam laser ablation of dielectrics," *Optics Letters*, vol. 35, no. 14, pp. 2490-2492, 2010.
- [48] E. Treacy, "Optical pulse compression with diffraction gratings," *IEEE Journal of Quantum Electronics*, vol. 5, no. 9, pp. 454-458, 1969.
- [49] F. Lukes, "Oxidation of Si and GaAs in air at room temperature," *Surface Science*, vol. 30, pp. 91-100, 1972.
- [50] D. von der Linde and K. Sokolowski-Tinten, "The physical mechanisms of short-pulse laser ablation," *Applied Surface Science*, Vols. 154-155, pp. 1-10, 2000.

- [51] G. Jellison Jr., "Optical functions of GaAs, GaP, and Ge determined by two-channel polarization modulation ellipsometry," *Optical Materials*, vol. 1, pp. 151-160, 1992.
- [52] T. Skauli, P. Kuo, K. Vodopyanoc, T. Pinguet, O. Levi, L. Eyres, J. Harris, M. Fejer, B. Gerard, L. Becouarn and E. Lallier, "Improved dispersion relations for GaAs and applications to nonlinear optics," *Journal of Applied Physics*, vol. 94, pp. 6447-6455, 2003.
- [53] A. R. a. M. Majewski, "Modelling the optical dielectric function of GaAs and AIAs: Extension of Adachi's model," *Journal of Applied Physics*, vol. 80, pp. 5909-5914, 1996.
- [54] J. Blakemore, "Semiconducting and other major properties of gallium arsenide," *Journal of Applied Physics*, vol. 10, p. R123, 1982.
- [55] A. Cavalleri, K. Sokolowski-Tinten, J. Bialkowski and D. von der Linde, "Femtosecond laser ablation of gallium arsenide investigated with time-of-flight mass spectroscopy," *Applied Physics Letters*, vol. 72, p. 2385, 1998.
- [56] A. Okano, J. Kanasaki, Y. Nakai and N. Itoh, "Electronic processes in laser-induced GaO emission and laser ablation of the GaP(110) and GaAs(110) surfaces," *Journal of Physics: Condensed Matter*, vol. 6, pp. 2697-2712, 1994.
- [57] K. Lim and M. Richardson, "Laser filamentation-beyond self-focusing and plasma defocusing," PhD Dissertation, CREOL, The College of Optics and Photonics, University of Central Florida, Orlando, FL, 2014.
- [58] E. Gamalay, A. Rode and B. Luther-Davies, "Ablation of solids by femtosecond lasers: Ablation mechanism and ablation thresholds for metals and dielectrics," *Physics of Plasmas*, vol. 9, no. 3, pp. 949-957, 2002.
- [59] A. Ben-Yakar, J. Ashmore, R. Byer and H. Stone, "Thermal and fluid processes of a thin melt zone during femtosecond laser ablation of glass: the formation of rims by single laser pulses," *Journal of Physics D: Applied Physics*, vol. 40, p. 1447, 2007.
- [60] J. Yoo, S. Jeong, X. Mao, R. Greif and R. Russo, "Evidence for phase-explosion and generation of large particles during high power nanosecond laser ablation of silicon," *Applied Physics Letters*, vol. 76, no. 6, p. 783, 2000.

- [61] X. Lv, Y. Pan, Z. Jia, Z. Li and X. Ni, "Surface damage induced by a combined millisecond and nanosecond laser," *Applied Optics* , vol. 56, no. 17, pp. 5060-5066, 2017.
- [62] B. Wu, Y. Zhou and A. Forsman, "Study of laser-plasma interaction using a physics-based model for understanding the mechanism of double-pulse effect in nanosecond laser ablation," *Applied Physics Letters*, vol. 95, no. 251109, 2009.
- [63] X. Wang, A. Michalowski, D. Walter, D. Sommer, M. Kraus, J. Liu and F. Dausinger, "Laser drilling of stainless steel with nanosecond double-pulse," *Optics & Laser Technology*, vol. 41, pp. 148-153, 2009.
- [64] X. Zeng, X. Mao, R. Greif and R. Russo, "Experimental investigation of ablation efficiency and plasma expansion during femtosecond and nanosecond laser ablation of silicon," *Applied Physics A*, vol. 80, pp. 237-241, 2005.
- [65] L. Sedov, "Propagation of strong blast waves," *Doklady Akademii nauk SSSR*, vol. 52, no. 17, 1946.
- [66] G. Taylor, "The formation of a blast wave by a very intense explosion," *Proceedings of the Royal Society*, vol. A201, no. 159, pp. 175-186, 1950.
- [67] Y. Qi, H. Gi, Q. Wang, Z. Chen and H. Zhan, "The influence of double pulse delay and ambient pressure on femtosecond laser ablation of silicon," *Optics Laser and Technology*, vol. 66, pp. 68-77, 2015.